energies

MDPI

Article

Parametric Study on the Flow Profiles of Vertical Sinter Cooling Bed Using the DEM and Taguchi Method for Waste Heat Recovery

Junpeng Fu * and Jiuju Cai

SEP (State Environment Protection) Key Laboratory of Eco-Industry, Department of Thermal Engineering, School of Metallurgy, Northeastern University, Shenyang 110819, China; rcjj@mail.neu.edu.cn

* Correspondence: 1210277@stu.neu.edu.cn

Received: 5 September 2020; Accepted: 22 September 2020; Published: 24 September 2020



Abstract: To comprehensively understand the effectiveness of external factors on flow characteristics and realize particle flow distribution evenly in bulk layers is an essential prerequisite for improving the performance of heat transfer in vertical sinter cooling beds (VSCBs). The numerical discrete element method (DEM) was applied to investigate external geometric and operational factors, such as the aspect ratio, geometry factor, half hopper angle, normalized outlet scale, and discharge velocity. Using the Taguchi method, a statistical analysis of the effect of design factors on response was performed. In this study, we focused more on external factors than granular properties, be remodelling the external factors was more useful and reliable for actual production in industries. The results showed that the most important factor was the aspect ratio, followed by the geometry factor, normalized outlet scale, half hopper angle, and discharge velocity for the dimensionless height of mass flow. In terms of the Froude number, the most influential factor was the normalized outlet scale with a contribution ratio of 33.81%, followed by the aspect ratio (22.86%), geometry factor (17.73%), discharge velocity (17.73%), and half hopper angle (11.83%).

Keywords: DEM; Taguchi method; flow profiles; VSCB

1. Introduction

The vertical sinter cooling bed (VSCB) is the principal device for cooling red-hot sinter granular compounds from the sintering machine during the production process in the industry. During the cooling process, a large amount of sensible heat is produced, which is expected to be recovered to reduce energy consumption and mitigate the environmental impact. During the past decade, a considerable number of research papers have been developed in the field of VSCB, mainly focusing on thermodynamics parameters, such as the solid and gas inlet temperature, solid and gas inlet mass flow rate, aspect ratio of VSCB [1–3], and gas pressure loss [4–6]. Moreover, optimization studies have examined the coefficient of heat transfer [7,8] and exergy transfer [9,10]. Previous research has demonstrated few effects on improving the performance of heat transfer in VSCB. In actual production, the challenge of engineering problems limiting the performance of heat transfer in VSCB remains unresolved, which includes the external aspect of the serious air pressure loss and inferiority equality of heat resource recovery, prohibiting effective heat transfer between air and sinter granular compounds, and a worse internal aspect of the sinter granular flow pattern. In general, the flow pattern of sinter granular material comprises two distinct flow types, such as the mass flow and funnel flow pattern. A good granular material flow profile is considered to have the greatest influence, guaranteeing efficient work for enhancing energy utilization and reducing the maintenance cost. Thus, a comprehensive understanding of the dynamic evolution of the flow pattern in VSCB has a significant effect on

improving the performance of heat transfer between air and sinter granular compounds. As reported in the literature, a numerical study of VSCB can simplify the conical silo structure, which is deemed a black box. Thus, information on the evolution of flow profile dynamics and the micro properties of inner granular compounds is very difficult to obtain. The conical silo structure has the advantages of a simple structure and ease of operation for extensive use. However, the behaviour of the granular material flow pattern inside the conical silo structure is complex, especially in VSCB, with a gas–solid counter-current flow in the heat transfer process. The granular flow pattern has a considerable influence on the even distribution of the gas–solid flow, thus optimizing the heat transfer between the cooling air and red-hot sinter material granular compounds. Therefore, investigating the effects of design factors on the evolution of sinter granular dynamics during the flow process to obtain the desired flow pattern is an important prerequisite for effectively improving the heat transfer performance in VSCB.

Efforts have been exerted on improving the granular flow performance in the vertical bed. Liu [11] investigated the effect of coke size segregation on the flow pattern in the coke dry quenching bed using a numerical and experimental method. Feng [12] showed that the descending behaviour was significantly influenced by internal friction, and the sluggishness of the cokes was dominated by external friction based on the 1/7 scale experimental model using the Navier–Stokes method. Yu [13] observed the effect of the opening radius and nut coke rate (NCR) on the coke discharge pattern and found that increasing the opening radius and NCR was beneficial for improving the blast furnace performance. Qiu [14] demonstrated the influence of the heat exchange tube and temperature of slag on the intensification of heat transfer in the blast furnace using a discrete element method (DEM) and revealed that tube number increased with a stagger configuration, and slag inlet temperature decreases were beneficial for enhancing heat transfer. Song [15] optimized the complex structures of the vent-cap to improve the gas and solid stable flow in the coke dry quenching bed, according to the aforementioned observed relationship of the flow pattern and performance of heat transfer in the confined structure device during the heat exchange between the gas–solid process. The dynamic evolution of the flow pattern is closely related to design factors, such as the height and diameter of the bed, hopper angle, and outlet dimension. A number of useful indirect research has demonstrated the effect of the flow pattern on the performance of the vertical bed; however, the effect of design factors on flow profiles in VSCB remains unclear. To improve the flow profiles, numerous efforts have been spent on investigating the mechanism of granular discharge in various geometric structures with different types of stored granular materials. Zhang [16] revealed the mechanism of the flow pattern critical transition using the DEM method based on the three-dimensional grain granular silo. Zeng [17] investigated the relationship between the silo quake and grain granular flow velocity and force fluctuation using DEM, and they found that the hopper angle and static friction between the grain and silo wall greatly influenced the velocity and force fluctuation of grain granular compounds. Han [18] observed the characteristics of methods for the determination of the flow pattern transition and analysed the reasons for the flow transition in discharge flow units. Fullard [19] applied experimental and particle image velocimetry (PIV) methods to investigate the velocity field of amaranth seeds within a flat-bottomed silo. Chen [20] investigated the flow pattern in a full-scale testing silo with iron ore pellets and established the relationship between the solid flow pattern and wall pressure distribution. Job [21] described a tracer method to observe the sugar flow pattern in a storage silo and found that the plug flow emerging only at the center of the perimeter volume of granular remained motionless. Previous investigations of the mechanism of the singular design factor on flow patterns have demonstrated the quality or quantity during the granular flow process. It is noteworthy that the flow pattern is determined by the combination of design factors simultaneously. Systematic research should be introduced to reveal the relationship between the flow pattern and design factors to comprehensively understand how individuals and the combination of design factors influence the flow pattern in VSCB. Furthermore, a statistical method was applied to obtain the optimal design factor combination for improving the performance of flow profiles in VSCB, in addition to enhancing the performance of heat transfer in VSCB in subsequent work.

The discrete element method (DEM) was used to investigate the effect of design factors, including the aspect ratio, geometry factor, normalized outlet scale, hopper half angle, and discharge velocity, on sinter granular flow profiles in VSCB. Design factors have an important influence on the variation in the flow pattern, in addition to impacting the performance of the heat transfer in VSCB. The aims of the present study were to investigate the effect of singular design parameters on the flow profile in VSCB to quantitively and qualitatively determine the mechanism underlying individual factors and the flow pattern. Next, we determined the most influential design factor on the flow profile and contribution ratio. Furthermore, the Taguchi method was applied to elucidate the optimal combination of design parameters to achieve an optimal performance of flow profiles determined by the dimensionless mass flow height and Froude number as target responses. The results of this research provided a combination of design parameters for optimizing the performance of the heat transfer process and the structural device of VSCB in future work.

2. Numerical Methodology

2.1. DEM Method

The discrete element method (DEM) is considered to be an effective tool to reveal the dynamic evolution of granular material in confined geometry, which was developed by Cundall and Strack [22]. To solve the related problems of the dynamic evolution of the sinter layer flow profile in VSCB, a three-dimensional DEM numerical model is applied to describe the dynamic behaviour of the sinter granular system containing two distinct types of motions of translational and rotational determined by Newton's second law. The DEM numerical method can dissect the integrity of the calculation domain into many different discrete sections with many shapes and masses. The properties of individual particles involve a discrete calculation method to simulate the entire varying behaviour of the whole system. Newton's second law is applied to describe the individual particle track and motion. The correlation of force and displacement in the occurrence at the contact point is described as follows:

Translational motion:

$$m_i \frac{dv_i}{dt} = m_i g + \sum_{i=1}^{n_i} (F_c^n + F_d^n + F_c^t + F_d^t) \quad (1)$$

Rotational motion:

$$I_i \frac{d\omega_i}{dt} = \sum_{i=1}^{n_i} (T_{t,ij} + T_{r,ij}) \quad (2)$$

The dynamic evolution of the sinter layer is determined by the Hertz–Mindlin [23,24] contact model, the force and torque of the contact of the sinter particle and sinter-wall are controlled by the no-slip Hertz–Mindlin model, and the change in the tangential and normal direction is modified by Mindlin-Deresiewic's theory and Hertz's theory, respectively. The details of the forces and torques of research objects and the correlation of their equations are described in Table 1.

Table 1. Forces and torques contained among particles *i* and *j*.

Parameters	Symbols	Equations
Normal contact force	${F_c}^n$	$\boldsymbol{F}_c^n = \frac{4}{3}E^*(r^*)^{1/2}\delta_n^{3/2}\mathbf{n}_{ij}$
Tangential contact force	${F_c}^t$	$\boldsymbol{F}_c^t = 8G^*\sqrt{r^*\delta_n}\mathbf{t_{ij}}\ (\delta_t < \delta_{t,max})$
Normal damping force	${F_d}^n$	$\boldsymbol{F}_d^n = -2\sqrt{\frac{5}{6}}\frac{\ln e}{\sqrt{\ln^2 e+\pi^2}}\sqrt{S_n m^* \boldsymbol{v}_{ij}^n}$
Tangential damping force	${F_d}^t$	$\boldsymbol{F}_d^t = -2\sqrt{\frac{5}{6}}\frac{\ln e}{\sqrt{\ln^2 e+\pi^2}}\sqrt{S_t m^* \boldsymbol{v}_{ij}^t}\ (\delta_t < \delta_{t,max})$
Torque by tangential forces	$T_{t,ij}$	$\boldsymbol{T}_{t,ij} = r_{ij} \times (F_c^t + F_d^t)$
Rolling friction torque	$T_{r,ij}$	$\boldsymbol{T}_{r,ij} = \mu_{r,ij}(\boldsymbol{F}_{c,ij}^n + \boldsymbol{F}_{d,ij}^n)\boldsymbol{\omega}_{t,ij}/\lvert\boldsymbol{\omega}_{t,ij}\rvert$

where $E^* = E/2(1-\upsilon^2)$, $1/m^* = 1/m_i + 1/m_j$, $1/r^* = 1/r_i + 1/r_j$, $1/G^* = (2-\upsilon_i)/G_i + (2-\upsilon_j)/G_j$, $\boldsymbol{v}_{ij} = \boldsymbol{v}_i - \boldsymbol{v}_j + \boldsymbol{\omega}_j \times r_{ij} - \boldsymbol{\omega}_i \times r_{ij}$, $S_t = 8G^*\sqrt{r^*\delta_n}$, $S_n = 2E^*\sqrt{r^*\delta_n}$.

2.2. DEM Geometry Model and Simulation Setup

The geometry of the VCSB contains two distinct domains, including the cylindrical and hopper sections. Parameters are used in DEM calculations, which are listed in Table 2. Figure 1 describes the details by which the conical structure of VCSB is established for experiments and calculations. There are four interchangeable hoppers with a hopper half angle of 30°–60° with a step of 10° in Figure 1a. The radius cross-section is located in the X-Y plane that divides the center section into ten equal calculated elements with a length of r_c equal to 0.1D. Figure 1b shows the configuration of the center cross-section in the X-Z plane with a slice thickness of 0.1D. The center cross-section of VCSB is evenly divided into 10 domains along the radius and height directions, respectively. The scale of the unit calculated element of the sinter layer is 0.1D in length, 0.1D in thickness, and 0.1H in height. The continuous filling process at the top of the free surface is limited, which disturbs the evolution dynamic parameters of the concerned sinter layer, including the velocity, kinetic energy, and contact force in the simulation. The calculated domain of the sinter granular layer of 0.1–0.8H from the zone converging on the cross-section between the cylindrical and hopper is positioned below the top surface of the sinter layer with a height of 0.8H.

Table 2. Parameters used in DEM calculation.

Parameters	Value
Particles static friction	0.3
Particles rolling fraction	0.1
Restitution between particles	0.15
Young's modulus/Pa	2.6×10^9
Poisson's ratio	0.25
Wall static frictional coefficient	0.2
Wall rolling frictional coefficient	0.15
Restitution between particles and wall	0.2
Young's modulus of wall	7×10^{10}
Poisson's ratio of wall	0.3

A variety of significant points should be noted in the following:

1. To distinguish different parts of the conical structure of VCSB, the coordinate system origin is located in the convergence zone between the cylindrical and hopper portions.
2. The walls of the conical structure consist of a rigid matter, forming an inflexible boundary that is used for preventing sinter granular compound penetration of the boundary during the simulation.
3. The criterion for deciding a sinter granular compound is located in the calculated unit element is that the center of the sinter granular material is situated in the unit element.
4. The rule of determining the scale of the unit element is that the selected dimension of the element is larger than the maximum diameter of the granular material located in the unit element.

2.3. Experimental Device and Method

Figure 1a shows a schematic of VSCB, which is applied to set-up for experimental testing, which is comprised of two distinct parts, including circle cylindrical and hopper. In order to validate the different situations of particle mass flow rate with the corresponding value of calculation, the interchanged hoppers are applied to modify the variation in half hopper angle. A pre-chamber arranged at the top of the cylindrical section is used to load a vertical packed bed with sinter particles. Sinter granular exports are performed with the help of a discharge device composed of an electromagnetism feeder and rotary sealed valve and driven by an electromotor. The combination of discharge devices is mainly employed to facilitate the exportation of sinter particles with uniform velocity. The inlet of the discharge system is applied to adjust the width of the outlet of the hopper section.

The sinter particles continuously pour from the top of the VSCB, forming the cone-shaped free surface, while the target filling height is reached, and the sinter granular filling process is temporarily paused. The sinter granular remains in a static state for ten minutes and is used to guarantee particles to accomplish redistribution between sinter layers and maintain stabilization. Then, the discharge device has initiated the sinter granular filling process and outlet opening simultaneously. The mass flow rate of sinter particles is recorded and measured by a computer and industrial weighting balance connected to the computer, respectively. The time interval of the discharge process is also recorded by the computer.

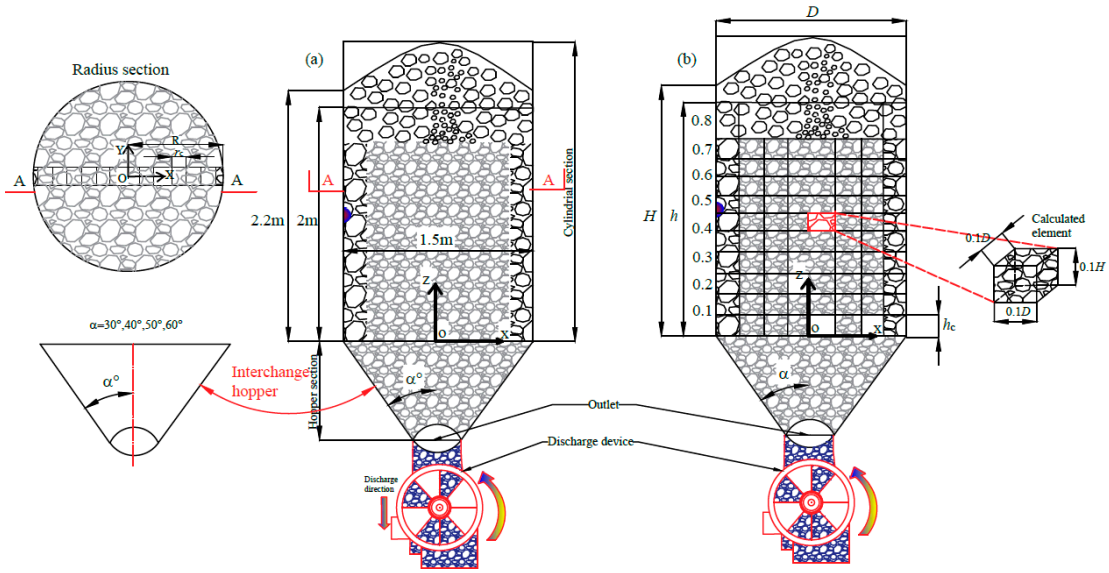


Figure 1. Schematic of the geometry used for (**a**) the experiment and (**b**) the numerical calculation.

3. Results and Discussion

3.1. Model Validation

The conical structure of VSCB is established to validate the reliability and accuracy of the DEM model used for simulation. A detailed schematic of the structural configuration is shown in Figure 2a. The agreement of the results in the calculation and measurement is determined by observing the evolution of the mass flow rate under the hopper half angle of different situations. Figure 2a shows that four interchangeable conical hoppers with four hopper half angles, including 30°, 40°, 50°, and 60°, are chosen for validation. It should be noted that the PIV technique is adopted following the tracks of the particle tracer step method to verify the accuracy of the calculation model in previous literature. However, PIV is a reasonable standard method for the gas and liquid sparse phase, which is not applicable to the solid dense phase. Therefore, macroscopic behaviour of the sinter granular material is selected as a distinguishing criterion to determine the consistency of the calculation and experiment, which is a reliable method for model validation because the variation in mass flow rate is a barometer of the dynamic characteristic of flow pattern evolution in VSCB. Mass flow rate is selected as a criterion for testing the reliability of the simulation compared with the experimental model.

Figure 2 shows the variation between the simulation and experimental sinter mass flow rate with different hopper half angles. Five experimental datasets are used for validation of the consistency of the calculation and experiment. The results demonstrate that the mass flow rate experience has a dramatic fluctuation that shows an enhanced intensity with an increasing hopper half angle. The main cause of the fluctuation of the mass flow rate is due to the formation and disintegration of the arch in the outlet during the discharge process. An increase in the hopper half angle increases leads to an obstruction of the granular flow and a greater effect of the arch on disintegration during the granular flow procedure.

Finally, the mass flow rate increases with time and then oscillates around the mean value of the mass flow rate. The mean value of the mass flow rate decreases with an increase in the hopper half angle. The average values of the mass flow rate are 11.9 kg/s, 10.8 kg/s, 9.8 kg/s, and 8.6 kg/s for 30°, 40°, 50°, and 60°, respectively.

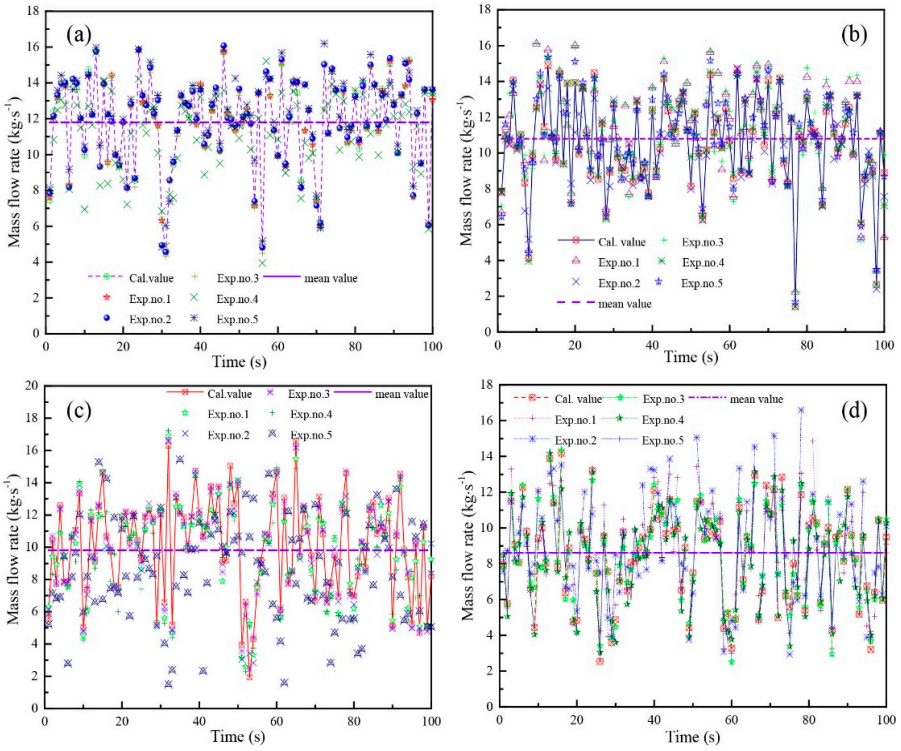


Figure 2. Comparison of the simulation and experimental sinter mass flow rate with different hopper half angles of (**a**) 30°, (**b**) 40°, (**c**) 50°, and (**d**) 60°.

Furthermore, a quantitative analysis of the deviation of the calculation and experiment is introduced to reveal the reliability and accuracy of the simulation model. Figure 3 shows a comparison of the results of the calculation and experiments for the hopper half angle in the range from 30–60° with an increasing step of 10°. The deviation of the calculation and experimental values increases with the increase in the hopper half angle, which is attributed to the oscillation of the mass flow rate intensified by the increase in the hopper half angle. As seen in Figure 2, the simulation value gradually deviates from the measured value with an increase in the hopper half angle; however, the deviation scale for predicting the relationship between the calculation and experiment is below 10% with four different measured situations. The results show a good agreement between the simulated and measured value. The error value between the calculated and measured value is determined by the equation. The mean error value of the simulated and measured value is 1.98%, 3.10%, 3.99%, and 4.88% for a hopper half angle of 30°, 40°, 50°, and 60°, respectively.

$$r = \frac{1}{n}\sum_{i}^{n}\left|\left(f_{cal,i} - f_{\exp,i}\right)/f_{\exp,i}\right| \times 100\% \quad (3)$$

where r is the error value, n is the total experiments, i is the ith experiment or calculation, $f_{cal,i}$ is the ith calculation result, and $f_{\exp,i}$ is the ith experimental result.

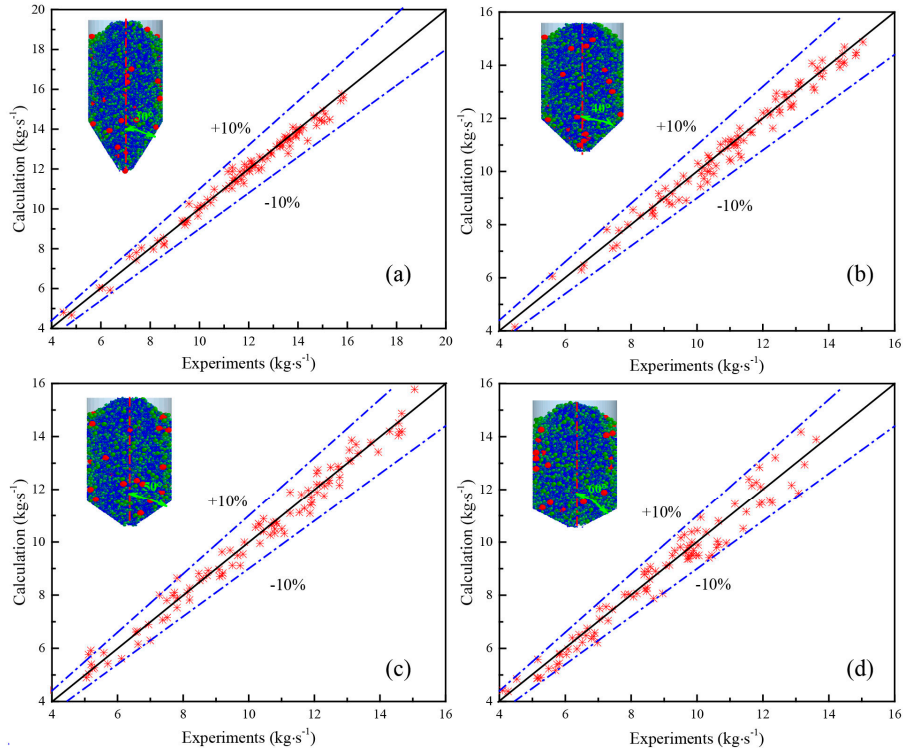


Figure 3. The deviation of the calculation and experimental value with different hopper half angles of (**a**) 30°, (**b**) 40°, (**c**) 50°, and (**d**) 60° using the Equation (3).

3.2. The Effect of the Aspect Ratio

3.2.1. The Effect of the Aspect Ratio on Flow Profiles

The aspect ratio is the ratio of the filling height to bed diameter (H/D_0), which is considered a significant factor that influences granular velocity profiles, while granular flow profiles have an important impact on the gas distribution and heat transfer in VSCB. Therefore, a comprehensive understanding of the variation in granular flow profiles is the top priority and challenge in research on the current difficult problem of the flow pattern during the gas–solid heat transfer process. The evolution of granular flow profiles of different aspect ratios during the export flow process in VSCB is studied. The vertical velocity (v_z) of the granular material is selected as a function of the normalized radius position (r_0/D_0) for different normalized sinter layer heights (H_0/H), as illustrated in Figure 4. The similarity trend is shown in Figure 4, where the maximum velocity occurs in the center of the flow panel, and the minimum velocity is present in the vicinity of the wall with different height layers. Moreover, the granular velocity increases with the decrease in sinter layer height in the center of the flow passage, and the variation in velocity near the wall is the opposite. The granular flow velocity in the center of the flow passage is clearly obstructed, and the magnitude of velocity dramatically decreases with an increasing aspect ratio. In contrast, the granular velocity close to the wall gradually increases with an increasing aspect ratio. It should be noted that the velocity of the granular material in the vicinity of the wall is dramatically reduced during the discharge process, which is beneficial for aggregating the formation of the dead zone near the wall and has a deleterious effect on increasing the velocity difference between the center and near wall section in Figure 4a. Figure 4d also shows that the fluctuation of granular velocity among all the sinter layers is substantially aggravated when the aspect ratio of VSCB is increased.

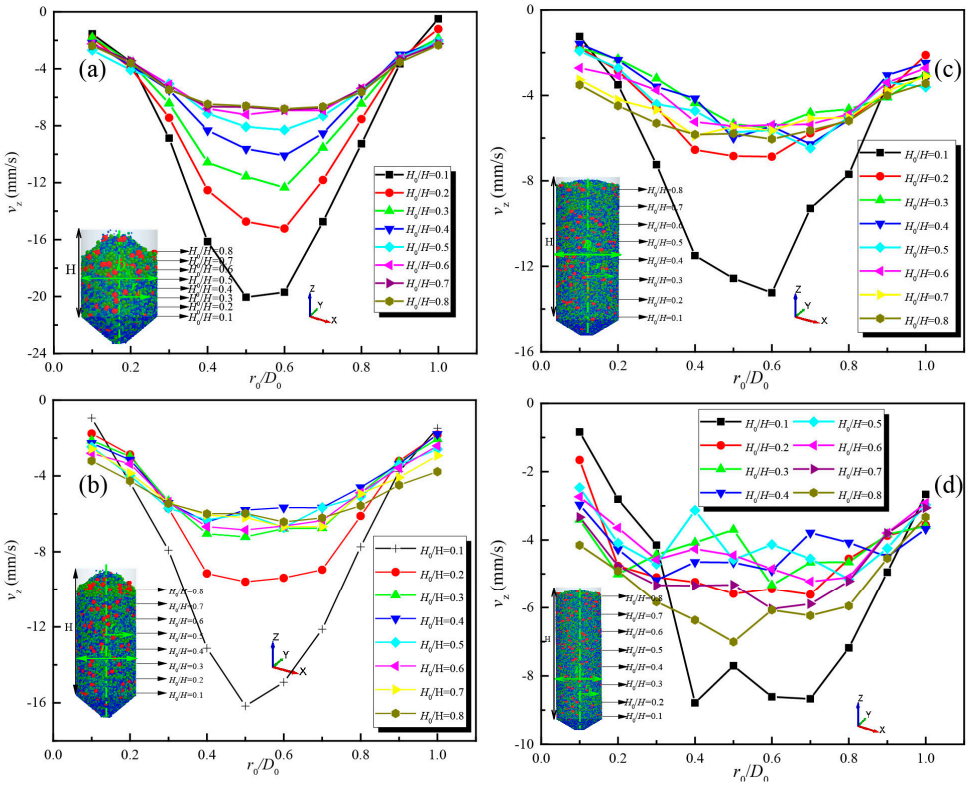


Figure 4. The variation in velocity profiles with different aspect ratios of (**a**) H/D_0 = 1, (**b**) H/D_0 = 2, (**c**) H/D_0 = 3, and (**d**) H/D_0 = 4.

In addition, the research is mainly focused on the switch in the variation in granular velocity in the center and near the wall section instead of the entire sinter layer. Figure 5 demonstrates the variation in granular velocity near the wall and in the center sections as a function of dimensionless filling height with different aspect ratios. In contrast, the granular velocity in the center witnesses a minimal decline in the range of aspect ratio from 1 to 3, and the corresponding magnitude for the granular velocity represents a steep decrease in the aspect ratio of 4. For the same sinter layers, the granular velocity near the wall experiences an overall trend that increases with the increasing aspect ratio. It should be noted that the granular velocity near the wall of the aspect ratio of 1 has a similar velocity distribution with the aspect ratio of 2. The corresponding velocity distribution in the aspect ratio of 4 with different layer heights has two distinct characteristics: a velocity distribution in the range of normalized filling height < 0.4 with an identical magnitude of the velocity with the evolution of velocity at the aspect ratio of 2; variation in the granular velocity in the range of normalized filling height > 0.4 very similar to the magnitude of the granular flow velocity at the aspect ratio of 3. Moreover, the difference in granular velocity between the center and near the wall is slightly reduced with the increase in aspect ratio; however, the velocity distribution of the aspect ratio of 4 continues to show a downward trend and a significant drop that damages the smooth flow of sinter granular material throughout VSCB.

Furthermore, the *MFI* (mass flow index) is introduced to describe the evolution of the flow pattern for quality and quantity analysis of the sinter particle flow performance. The criterion for determining the transition in the granular flow pattern with the help of *MFI* is as follows: *MFI* > 0.3 is the mass flow pattern, below which the flow pattern transitions from mass to funnel flow. The *MFI* is determined by the ratio of granular velocity near the wall and central section, and the equation for the mass flow index (*MFI*) is illustrated as follows.

$$MFI = \frac{v_w}{v_c} \tag{4}$$

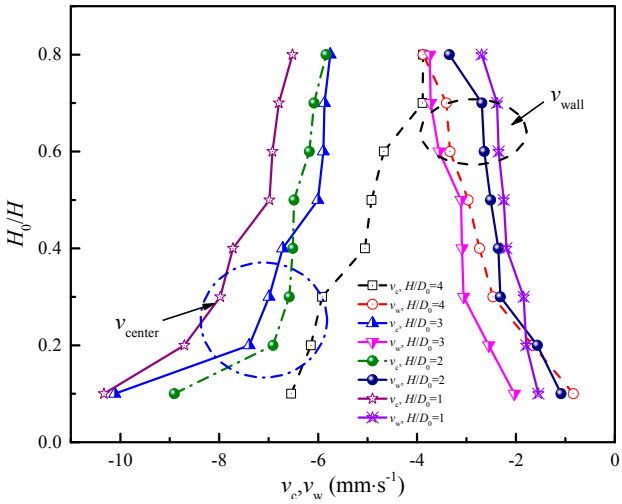


Figure 5. Variation in granular velocity near the wall and in the center of the flow passage with different sinter layers.

Figure 6 demonstrates that the evolution of *MFI* in the range of aspect ratio 1–3 presents a similar overall trend. From a normalized filling height onwards, the value of *MFI* starts to increase with minor fluctuations, while that in the aspect ratio of 4 gradually increases to nearly 0.6 at the normalized filling height in 0.5, after which it is projected to continue its upward trend more intensely to almost 1 by the top of the filling height. Figure 6 shows that the aspect ratios of 4 and 2 have nearly the same mass flow height (the height between the top of the filling height and the position of the flow pattern transition), showing nearly 70% of the total filling height. Regarding mass flow height, the aspect ratio of 3 presents the highest rate of 90% of the total filling height, while the corresponding value for the aspect ratio of 1 displays a mere 45% of the total filling height.

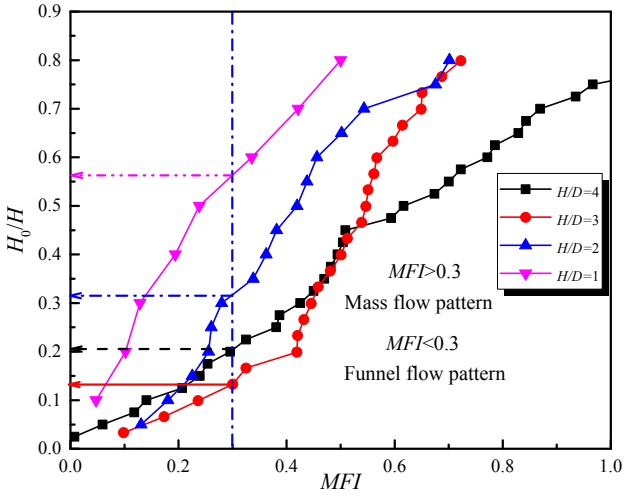


Figure 6. Variation in mass flow index (*MFI*) as a function of normalized sinter layers for different aspect ratios.

To comprehensively understand the dynamic evolution of the flow pattern in sinter layers, the velocity uniformity index (*VUI*) is introduced to represent the difference between each sinter layer's instantaneous velocity and that of the average value. Therefore, the uniformity of the granular velocity distribution is quantified by investigating the deviation of different sinter layers. Figure 7 shows the variation in *VUI* as a function of normalized filling height with different aspect ratios. The aspect ratios of 4 and 1 are almost the same in terms of the distribution of *VUI* along with the entire sinter layer,

and the corresponding variation in *VUI* for the aspect ratio of 2 shows a flow transition at normalized filling height 0.4, while the magnitude of *VUI* fluctuates slightly between normalized filling height 0.4 and 0.8 prior to a significant increase lower than the normalized filling height 0.4, almost approaching the maximum value of *VUI* in the aspect ratio of 4. Figure 7 shows that the magnitude of *VUI* in the aspect ratio of 2 is somewhere in the vicinity of 2-fold more than that of the aspect ratio of 3. Conversely, the variation in the *VUI* of the aspect ratio of 3 experiences an increase, only marginally between the normalized filling height (H_0/H) of 0.2 and 0.8 prior to a marked increase in the magnitude of *VUI* below the transition point at a normalized filling height (H_0/H) of 0.2. An equation is applied to show the unfolding of *VUI*.

$$VUI_j = \sqrt{\frac{\sum_{k=1}^{m} (v_{jk} - v_{ave,j})^2}{m-1}} \tag{5}$$

$$v_{jk} = \frac{\sum_{r=1}^{s} v_r}{s} \tag{6}$$

$$v_{ave,j} = \frac{1}{m}\sum_{k=1}^{m} v_{jk} \tag{7}$$

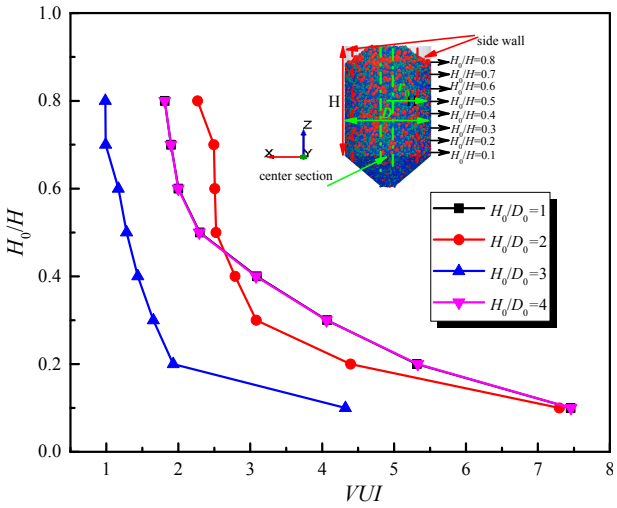


Figure 7. Evolution of velocity uniformity index (*VUI*) in sinter layers with different aspect ratios.

3.2.2. The Effect of the Aspect Ratio on Mass Discharge

The variation in mass discharge is deemed as a barometer to indicate the flow pattern problem in VSCB because the complexity of the evolutionary dynamics of the flow pattern is notably related to the lack of effective measures to obtain some crucial parameters as an indicator of the dynamic features of the sinter granular flow pattern. To offer an elaborate effect of the aspect ratio on the performance of the granular discharge process, the scope of the aspect ratio research is extended. Figure 8 reveals a comparison of the cumulative mass as a function of time with different aspect ratios in the range from 0.5 to 5. The general trend of mass discharge with time is that the amount of mass export increases steadily with testing time. Figure 8 shows that the value of mass export in the aspect ratio of 3 is significantly higher than the corresponding value of the other five aspect ratios. The aspect ratios of 2, 4, and 5 are almost the same in mass discharge, and the results for mass discharge with different aspect ratios show the lack of a positive correlation between improving the flow pattern and the increasing aspect ratio. The quantity of mass discharge experiences a significant rise from the aspect ratio of 0.5 to 3, followed by a marked drop above the aspect ratio of 3. The above-mentioned phenomenon presents

that a strategy to improve the flow pattern performance is merely dependent on increasing the filling height of VSCB, which is not an advisable choice.

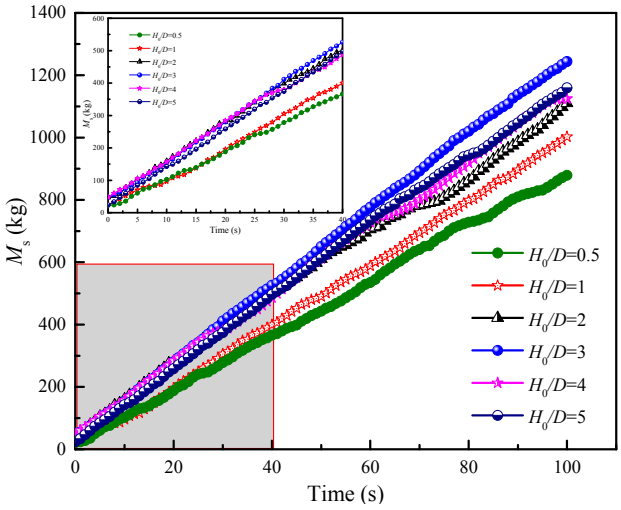


Figure 8. The cumulative mass with the measuring time for different aspect ratios.

3.2.3. The Effect of the Aspect Ratio on Shear Rate

The shear rate is deemed as a significant parameter of the rheological properties of sinter granular material. The dynamic evolution in the sinter packed bed has three functions: determination of the radial flow passage boundary between the static and flow sinter granular; quantification of the granular flow difficulty index, which represents the relative flow difficulty of different sinter layers in the radius flow passage, illustrating the reason for the variation in flow profiles in sinter layers. Thus, the transient particle flow is illustrated [25,26], showing the strength of the shear rate as an important parameter, determining the mode of particle transformation from static to dynamic. In this section, the variation in shear rate represents an indicative of sinter granular radius flow profile variation for different heights of sinter layers in VSCB. Figure 9 shows the increase in the magnitude of the shear rate with the increase in the radius position in close vicinity to the boundary wall and height of the sinter layer. The evolution of the magnitude of shear stress illustrates the degree of difficulty of flow in the radius section with different heights of sinter layers, which is mainly due to the friction between the sinter granular material and the boundary wall increase. While the dynamics of the flow transfer from the bottom to top sinter layers lead to increases in flow difficulty with the increasing height of the sinter layer. Figure 9 also demonstrates that the shear rate of sinter layers gradually decreases up to the aspect ratio of 3 and increases again with an increasing aspect ratio. The shear rate of sinter layers corresponding to the velocity profiles varies with different aspect ratios. A detailed description of the shear rate is observed as follows. The invariant second shear rate serves as a tensor, representing the quantitative evolution of shear rate:

$$\gamma_{ij} = \frac{\partial u_i}{\partial x_j} + \frac{\partial u_j}{\partial x_i} \tag{8}$$

$$\left|\gamma^*\right| = \sqrt{\frac{1}{2}\gamma_{ij}\gamma_{ij}} \tag{9}$$

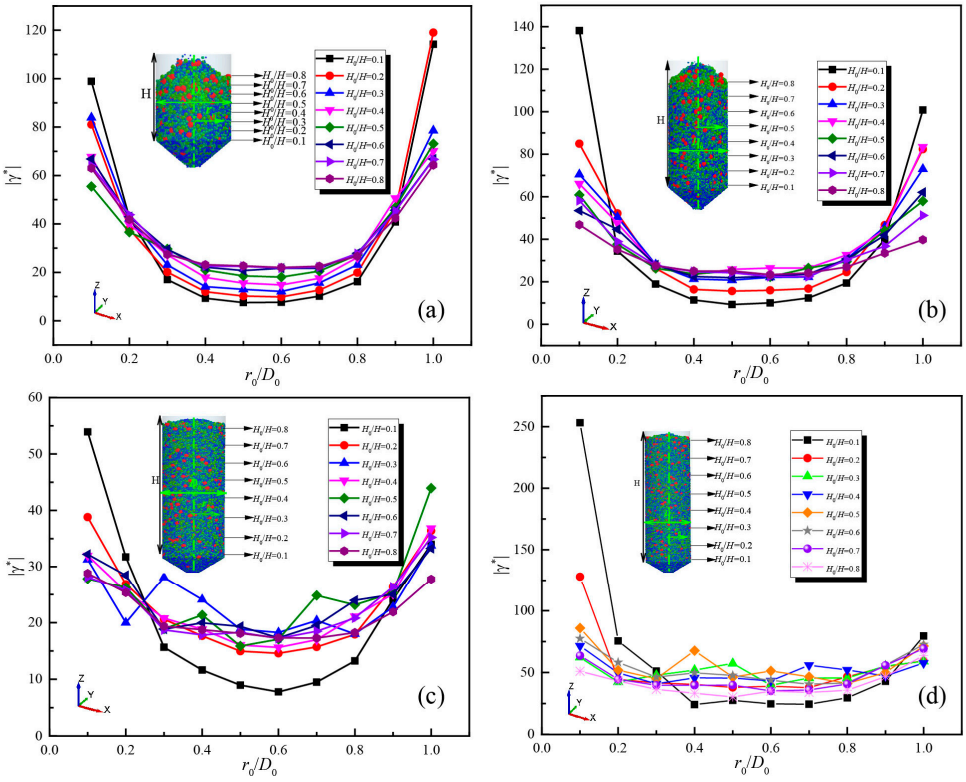


Figure 9. The variation in the shear rate tensor of the radius range for the entire sinter layers with different aspect ratios of (**a**) H/D_0 = 1, (**b**) H/D_0 = 2, (**c**) H/D_0 = 3, and (**d**) H/D_0 = 4.

3.3. The Effect of the Outlet Dimension

3.3.1. The Effect of the Outlet Dimension on the Flow Profiles

The evolution of the velocity of sinter layers as a function of radius position with different normalized outlets (d_0/D_0) is shown in Figure 10. The normalized outlet (d_0/D_0) is the ratio of the outlet of VSCB (d_0) to the diameter of VSCB (D_0). Figure 10 demonstrates that the velocity of the sinter layers increases with an increase in the normalized outlet and a decrease in the height of the sinter layers. It is possible that the obstruction of the contraction part is reduced with the increase in the normalized outlet. In addition, the velocity of the central region and region close to the sidewall dramatically increases with an increase in the normalized outlet, especially in the magnitude of the velocity with an increasing rate of the central part higher than that of the sidewall section. Therefore, the magnitude of the velocity difference between the central region and close to the wall section gradually increases with the aspect ratio onward. It should be noted that the variation in the velocity of sinter layers undergoes a tremendous fluctuation at a normalized outlet equal to 1, and the behaviour of the dynamic evolution of velocity has a negative effect on the smooth sinter layer flow export. Moreover, the difference in the variation in the velocity of sinter layers in normalized outlets between 3 and 4 is extremely small.

The variation in the magnitude of the velocity of the sidewall and central part of VSCB is a function of the height of sinter layers with different normalized outlet scales, as shown in Figure 11. Figure 11 illustrates the variation in the velocity of the sidewall section, which gradually increases with an increase in the normalized outlet. The magnitude of velocity in the vicinity of the wall at a normalized outlet of 0.3 and 0.4 remains nearly unchanged, which is three-fold and two-fold the magnitude of velocity at a normalized outlet of 0.1 and 0.2, respectively. In terms of the variation in the magnitude of velocity in the central part of VSCB, the magnitude of the velocity increases sharply with the increase in the normalized outlet and decrease in the height of the sinter layer. A similar variation in the magnitude of velocity in the central part of the sinter layers between the normalized outlet of 0.3

and 0.4 is recorded. The magnitude of velocity in the center part of the sinter layers is approximately 4 and 2 times the corresponding figure of the normalized outlet of 0.1 and 0.2, respectively. The difference between the variation in the magnitude of velocity in the vicinity of the wall and the center of the flow passage shows a dramatic increase with the normalized outlet increase, and the trend is mirrored in the corresponding results shown in Figure 10.

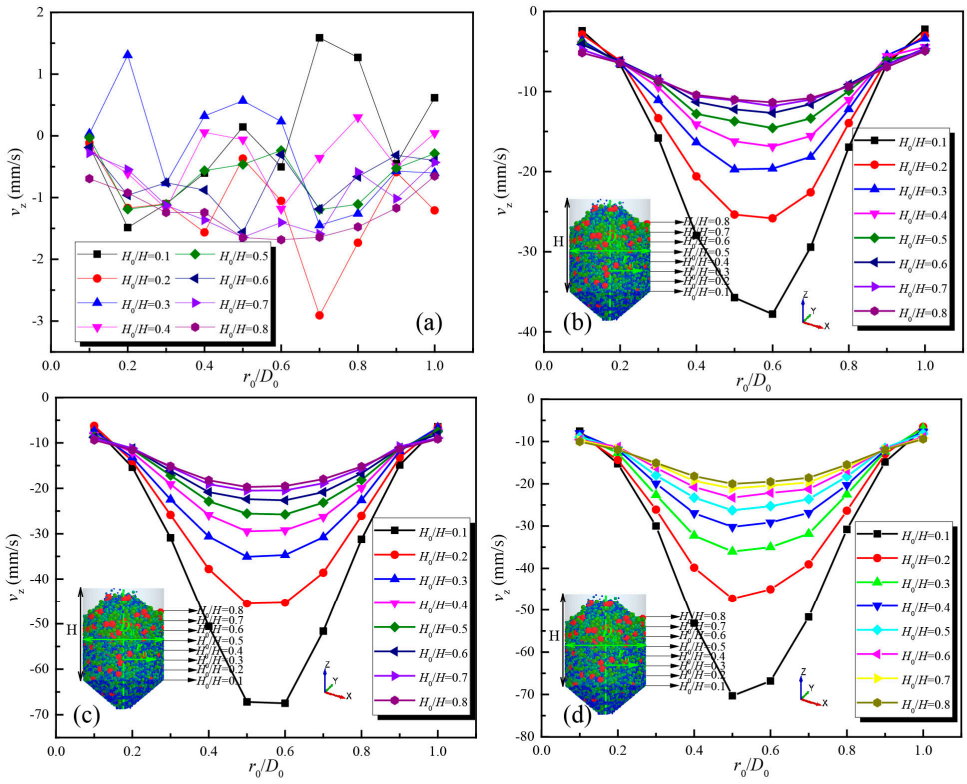


Figure 10. The variation in sinter layer velocity with different normalized outlets of (**a**) d_0/D_0 = 0.1, (**b**) d_0/D_0 = 0.2, (**c**) d_0/D_0 = 0.3, and (**d**) d_0/D_0 = 0.4.

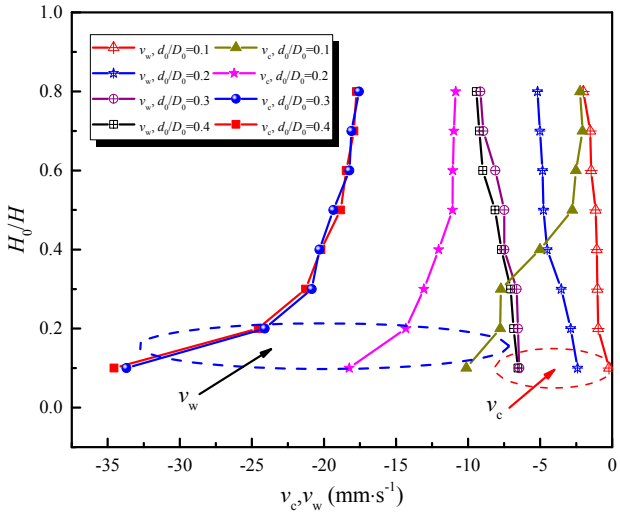


Figure 11. The evolution of sinter layer velocity along the vertical direction with different normalized outlet scales.

Figure 12 shows the variation in the *MFI* distribution in sinter layers with different normalized outlets. The transition position of the height of the sinter layer decreases with the increase in the normalized outlet while defining the *MFI* equal to 0.3 as an indicator of the transformation of flow pattern. In addition, the height of the mass flow in the normalized outlet equal to 0.2 is 2 times the height of the normalized outlet equal to 0.1. With respect to the height of the mass flow of the normalized outlet equal to 3 and 4, the height of the mass flow continues to show a slight increase as the rate of increase gradually slows down. The results for the variation in the height of mass flow show that the gap in the height of mass flow in sinter layers between normalized outlets equal to 4 and 2 is evidentially small.

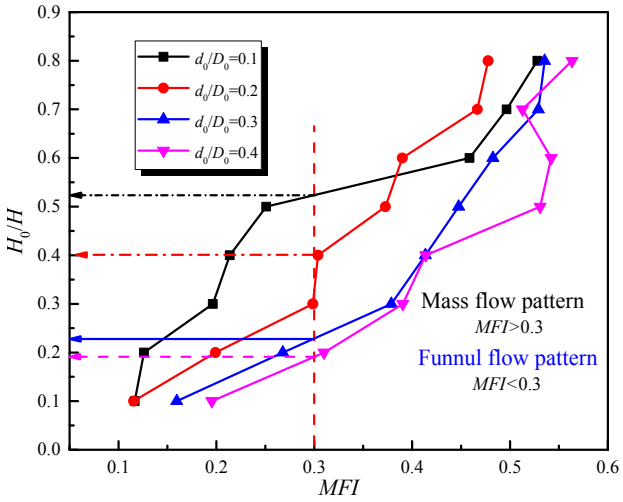


Figure 12. The variation in *MFI* in sinter layers with different normalized outlet scales.

Figure 13 depicts the evolution of *VUI* in sinter layers with different normalized outlet scales. The *VUI* in different sinter layers dramatically increases with the increases in normalized outlet scales and decreases in height of the sinter layer. The value of *VUI* in all sinter layers is less than 1 for a normalized outlet equal to 1. The variation trend and magnitude of *VUI* in the normalized outlet of 3 are fairly similar to that of the normalized outlet of 4, which is greater than the corresponding value of *VUI* in the normalized outlet of 2.

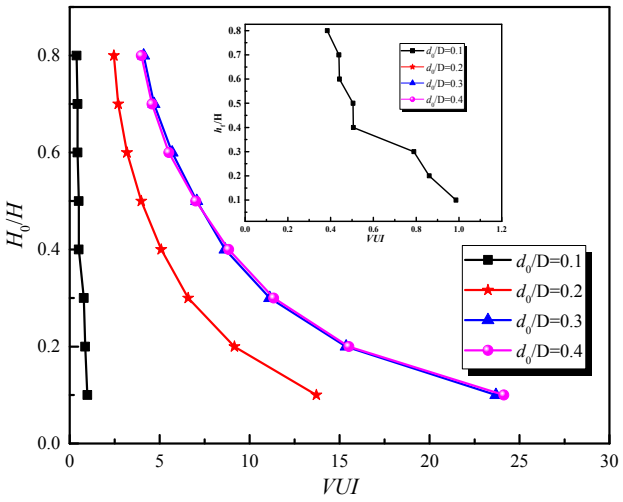


Figure 13. The variation in *VUI* in sinter layers with different normalized outlet scales and inset. *VUI* varies with sinter layers at the normalized outlet equal to 1.

3.3.2. The Effect of the Normalized Outlet Scale on Mass Discharge

Figure 14 represents the cumulative export mass as a function of operating time for different normalized outlet scales. The inset image shows the variation in cumulative mass for a normalized outlet lower than 0.2, in which the magnitude of mass flow export experiences a marginal rise with operating time onward, and the quantity of cumulative mass discharge (0.15 for the normalized outlet scale) is nearly three-fold that of the mass export of 0.1 for the normalized outlet scale. Figure 14 shows the magnitude of mass export dramatically increases with an increasing normalized outlet. The normalized outlet scales with 0.3 and 0.4 are almost identical in comparison to the cumulative mass export. The value of cumulative mass discharge of 0.3 for the normalized outlet scale remains two and three-fold that of the cumulative mass discharge of 0.25 and 0.2 for the normalized outlet scale, respectively.

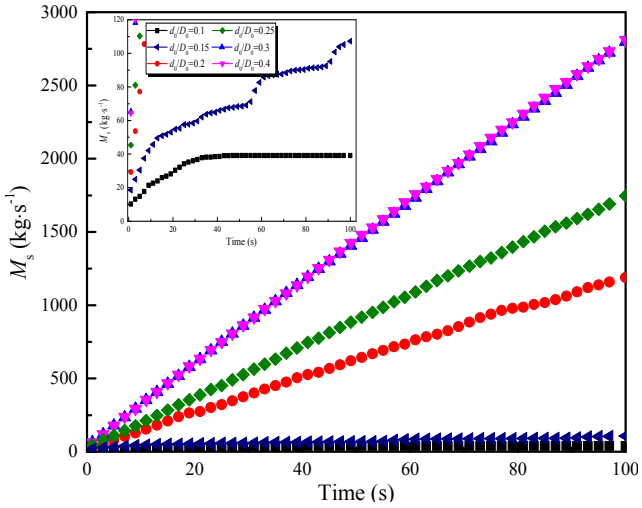


Figure 14. The variation in cumulative mass discharge with operating interval time for different normalized outlet scales and inset: the variation in cumulative mass export with the normalized outlet of 0.1 and 0.15.

3.3.3. The Effect of the Normalized Outlet Scale on Shear Rate

Figure 15 clearly shows that the design of the normalized outlet scales can effectively reduce the impact of particles and sidewall resistance and drag on the sinter granular flow through the passage of VSCB. In terms of the size of outlets smaller than the standard design limitation of the device, a steep flow fluctuation appears in particle layers, leading to the stabilization of extremely destroyed sinter layers, as presented in Figure 15a. With the increase in normalized outlet scales, the performance of flow profiles gradually improves in both central and sidewall sections of different sinter layers due to the effect of the normalized outlet scale on reducing the friction of both particles and sidewall with flow sinter layers simultaneously. Therefore, the magnitude of the shear rate shown in Figure 15b–d contains a steady decreasing trend in both central and sidewall sections with an increase in normalized outlet scale.

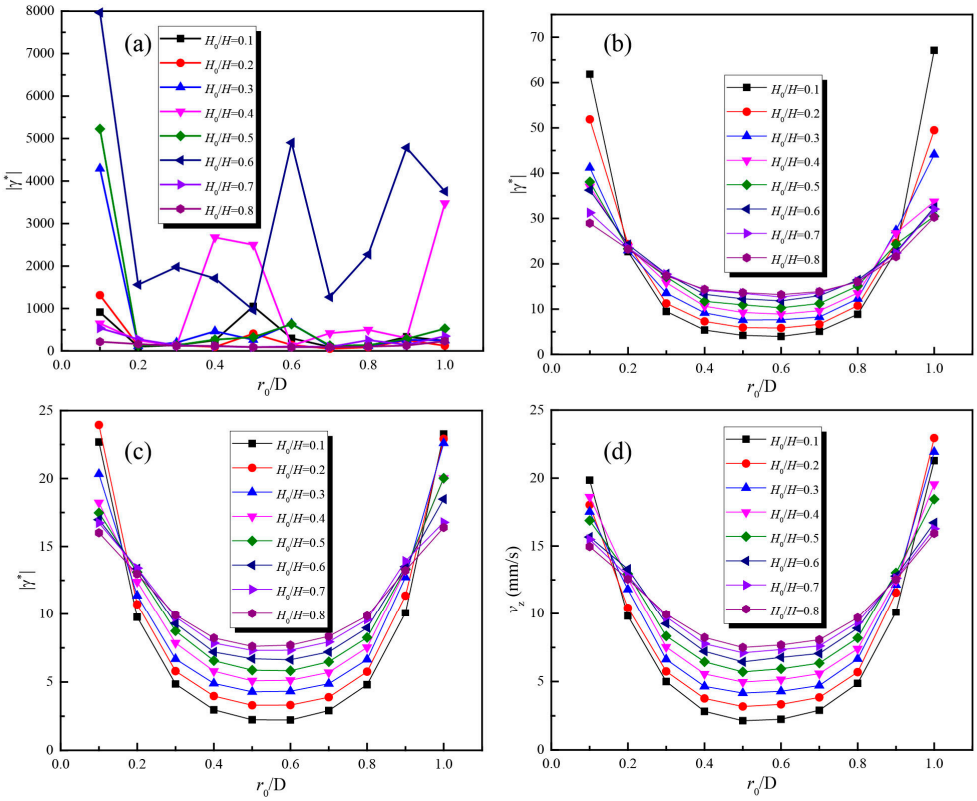


Figure 15. The variation in shear rate in sinter layers with different normalized outlet scales of (**a**) d_0/D_0 = 0.1, (**b**) d_0/D_0 = 0.2, (**c**) d_0/D_0 = 0.3, and (**d**) d_0/D_0 = 0.4.

3.4. The Effect of the Half Hopper Angle

3.4.1. The Effect of the Half Hopper Angle on Flow Profiles

The variation in velocity profiles of sinter layers for different half hopper angles is described in Figure 16, which shows that the velocity distribution in the sidewall section gradually decreases with increases in the half hopper angle and that an increased rate of velocity slightly slows down with half hopper angle onward. Conversely, the performance of velocity in the central section experiences an acceleration with the increase in the half hopper angle (except the evolution of velocity in the central section for a half hopper angle of 50°, which shows a slightly decreasing trend in the central section). According to the above-mentioned variation trend of the velocity distribution of sinter layers, the magnitude of velocity differs between the increases in central and sidewall sections with the increase in half hopper angle. The main effects of the half hopper angle on the velocity profiles of sinter layers are an accelerating velocity of the center part and deceleration of the corresponding value at the sidewall section.

In addition to a comprehensive evaluation of the variation in the velocity distribution in the central (v_c) and sidewall parts (v_w), the location in the center section and sidewall of sinter layers is considered a main focus in the research domain for different half hopper angles. Figure 17 demonstrates that the magnitude of velocity in the vicinity of the sidewall gradually decreases with increases in the half hopper angle and decreases in the height of the sinter layer, while that of the variation in velocity in the center section presents an opposite trend: the magnitude of the velocity increases with the increase in the half hopper angle and the height of the sinter layer. It should be noted that the different values of velocity between the central and sidewall sections grow steeply with the decrease in the height of the sinter layer, while the flow pattern of the sinter layer experiences a transition from mass flow to funnel flow.

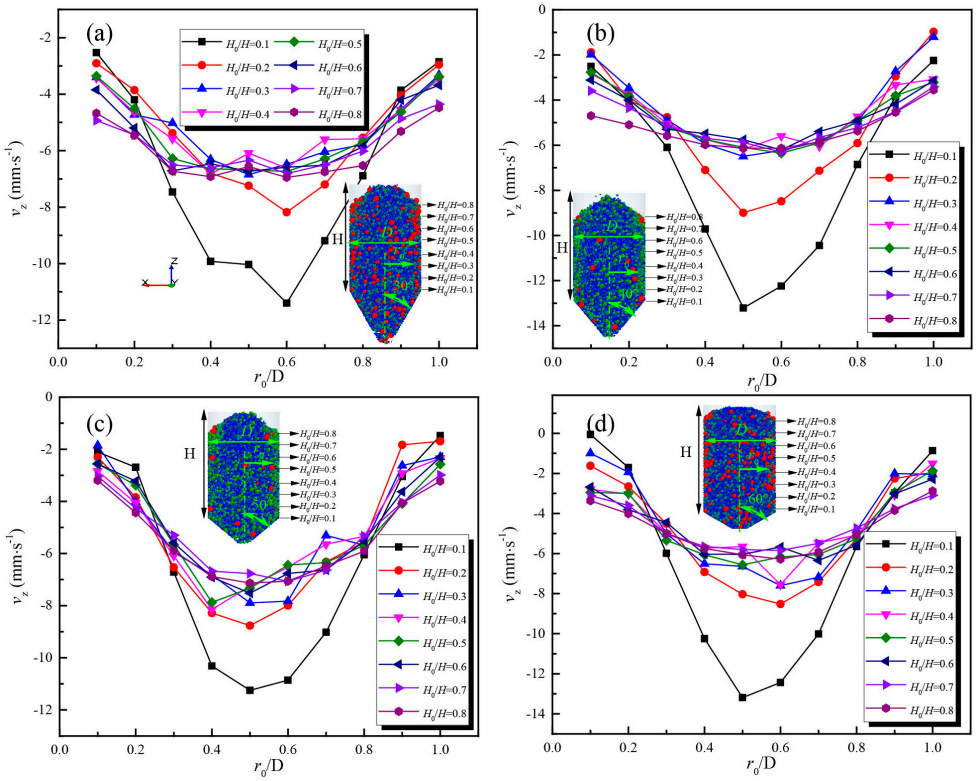


Figure 16. The variation in velocity profiles of sinter layers for different half hopper angles of (**a**) 30°, (**b**) 40°, (**c**) 50°, and (**d**) 60°.

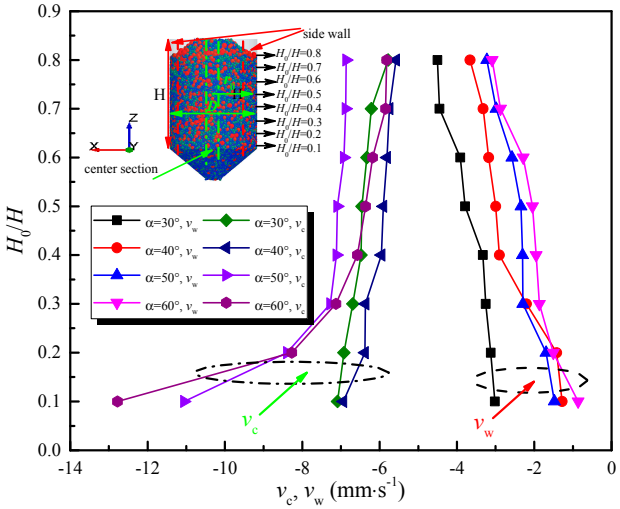


Figure 17. The variation in v_c, v_w with sinter layers for different half hopper angles.

To understand the variation in the flow pattern of the sinter layer comprehensively, *MFI* (mass flow index) is introduced to present the dynamic transition of the flow pattern of the sinter layer during the gas–solid heat transfer process. *MFI* is a significant parameter applied to quantitatively and qualitatively determine the flow pattern of the sinter layer during the transition of the flow pattern. Figure 18 illustrates the variation in *MFI* as a function of the dimensionless height of the sinter layer for half hopper angle variations. It is evident that the height of the flow pattern in transition increases with increases in the half hopper angle, and the disparities between the magnitude of velocity in the vicinity of the sidewall and central section become greater with increases in the half hopper angle.

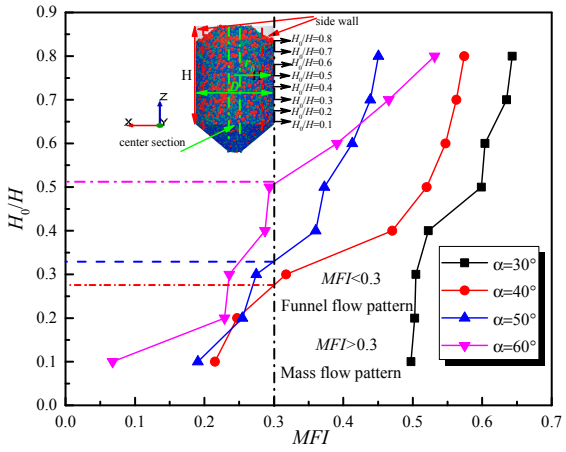


Figure 18. The variation in *MFI* with sinter layers for different half hopper angles.

The velocity uniform index (*VUI*) is used to unfold the difference in velocity distribution at identical heights of the sinter layer. A lower value of *VUI* presents better stability of the velocity distribution in the sinter layer and is beneficial for the steady flow pattern. Figure 19 illustrates the variation in *VUI* as a function of the dimensionless height of the sinter layer with a varying half hopper angle. The value of *VUI* sharply increases with an increase in half hopper angle and a decrease in the dimensionless height of the sinter layer. The variation trend of velocity illustrates the significant fluctuation in the lower part of VSCB and the large value of the half hopper angle. The overall trend of the change in velocity in the vicinity of the sidewall declines, and the corresponding value for the central section steeply accelerates with an increase in the half hopper angle, leading to a substantial fluctuation in the magnitude of *VUI* with a varying half hopper angle.

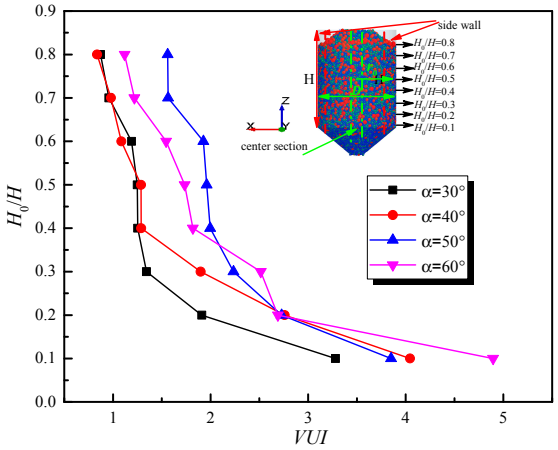


Figure 19. The variation in *VUI* with sinter layers for different half hopper angles.

3.4.2. The Effect of the Half Hopper Angle on Mass Discharge

Figure 20 demonstrates the change in mass flow during the discharge process with variations in the half hopper angle; the cumulative mass flow discharge slightly increases with operating time onward and a decrease in the half hopper angle. It is possible that the mass flow of the particles close to sidewall is constrained, leading to an inevitable decrease in the cumulative mass discharge with an increase in the half hopper angle, but the rate of decrease in mass flow is reduced due to the capacity of half hopper angle restriction on variations in the decrease in velocity in the vicinity of the sidewall with an increase in the half hopper angle.

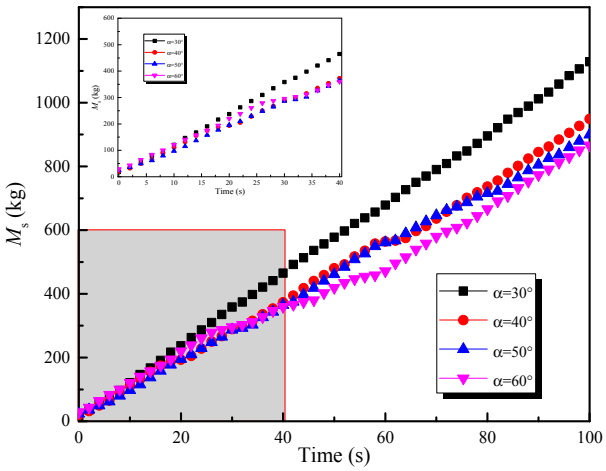


Figure 20. The variation in mass discharge with operating time for different half hopper angles.

3.4.3. The Effect of the Half Hopper Angle on Shear Rate

The quantitative effect of the half hopper angle on the variation in the shear rate of sinter layers reveals the variation in the shear rate of sinter layers as a function of the normalized radius position for different half hopper angles, as described in Figure 21. The variation in shear rate in the central section gradually decreases with an increase in the half hopper angle, so it is possible that the magnitude of velocity rises steeply with variations in the half hopper angle. The variation in shear rate in the vicinity of the sidewall results from the magnitude of the dramatic decline in velocity, leading to an increase in flow difficulty through the passage between sinter particles and the sidewall. The shear rate value shows marked growth with the increase in the half hopper angle, revealing the possibility of an increase in the funnel flow pattern and dead zone along the radius direction with enlargement of the half hopper angle.

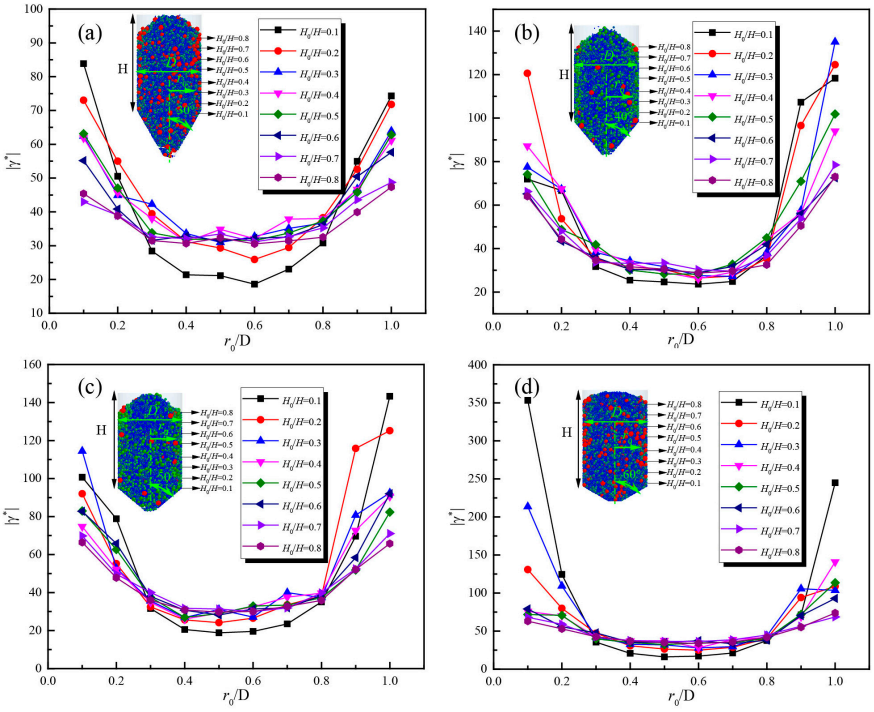


Figure 21. The variation in the shear rate of sinter layers with variations in the half hopper angles of (**a**) 30°, (**b**) 40°, (**c**) 50°, and (**d**) 60°.

3.5. The Effect of the Geometry Factor of VSCB

3.5.1. The Effect of the Geometry Factor on Flow Profiles

The geometry factor is a ratio of the diameter of VSCB (D_0) and average particle diameter (d_p), revealing the relationship of the scale factor of the external geometry parameter of VSCB and the diameter distribution of particles. Figure 22 illustrates the combination of the geometry parameter of VSCB and particle distribution influence on the performance of sinter layer flow profiles with variations in the geometry factor. The magnitude of the velocity of the sinter layers rises steeply with an increase in the geometry factor for the central section of the sinter particle flow passage and the lower part of the height of the sinter layers. Regarding the variation in velocity in the vicinity of the sidewall, the magnitude of velocity gradually decreases with an increase in the geometry factor, while the difference in the magnitude of velocity between the central and sidewall section becomes enlarged with the increase in the geometry factor.

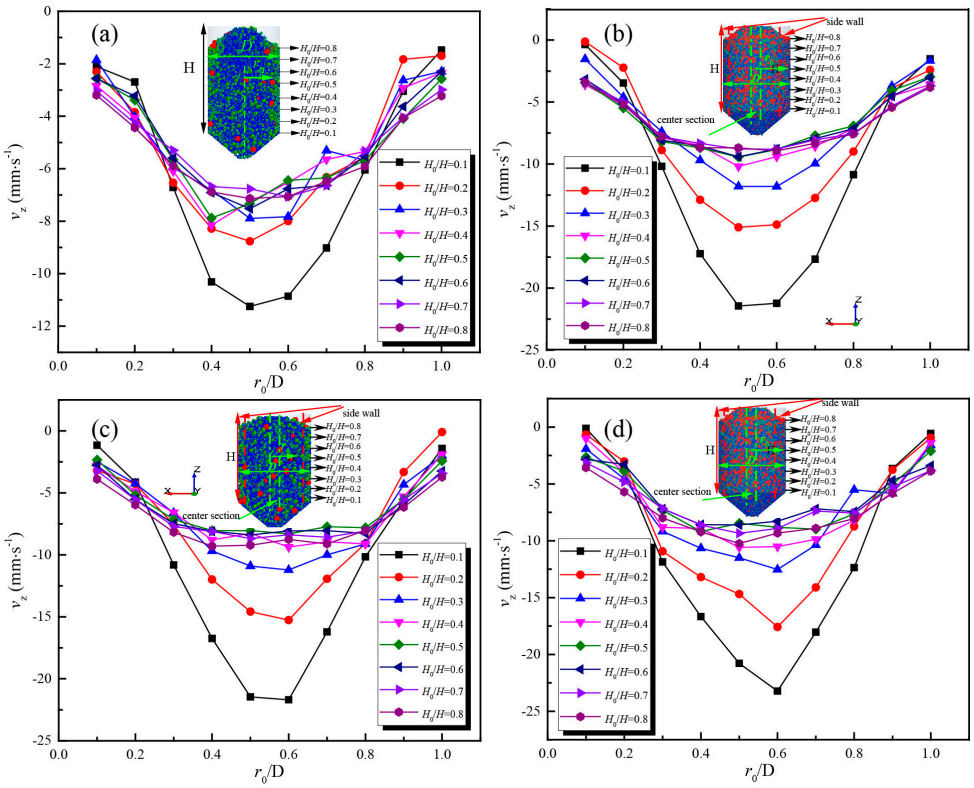


Figure 22. The variation in the velocity profile with sinter layers for different geometry factors of (**a**) D_0/d_p = 75, (**b**) D_0/d_p = 100, (**c**) D_0/d_p = 125, and (**d**) D_0/d_p = 150.

To investigate the effect of the geometry factor on the velocity distribution in sinter layers, the research is focused on the variation in velocity at the central and sidewall section of the flow passage of VSCB. Figure 23 presents the variation in v_c and v_w with sinter layers for different geometry factors at the central and sidewall section, respectively. The variation in the magnitude of velocity is evident in the vicinity of the sidewall; the magnitude of the velocity steeply decreases with increases in the geometry factor, and the rate of decrease undergoes an acceleration with the increase in geometry factor. With respect to the corresponding velocity at the central section, the magnitude of velocity sharply increases with an increase in the geometry factor, and the rate of the increase exhibits a dramatic rise with an increase in the geometry factor. The difference in magnitude of velocity between central and sidewall sections shows a marked rise with the increase in the geometry factor and decrease in the dimensionless height of sinter layers.

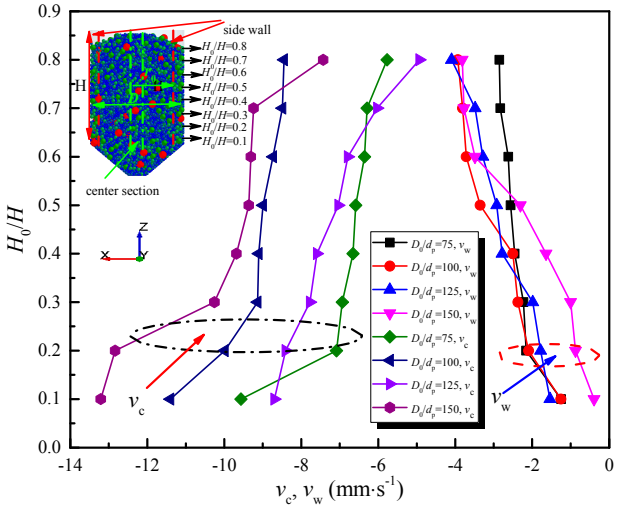


Figure 23. The variation in v_w, v_c along the height of sinter layers with variations in the geometry factor.

To analyse the stability of the velocity distribution within the sinter layers, the variation in *VUI* of sinter layers with variations in the geometry factor is illustrated in Figure 24. The magnitude of *VUI* clearly increases with an increase in the geometry factor and decreases in the dimensionless height of the sinter layers. The magnitude of the increase in *VUI* presents a disruption of the stabilization and uniformity of the velocity distribution of sinter layers, leading to the magnitude of variance between the velocity distribution of sinter layers and the corresponding dramatic increase in the value of the mean statistical velocity. Therefore, the flow pattern transition commences at the position of the steep rise in the magnitude of *VUI*.

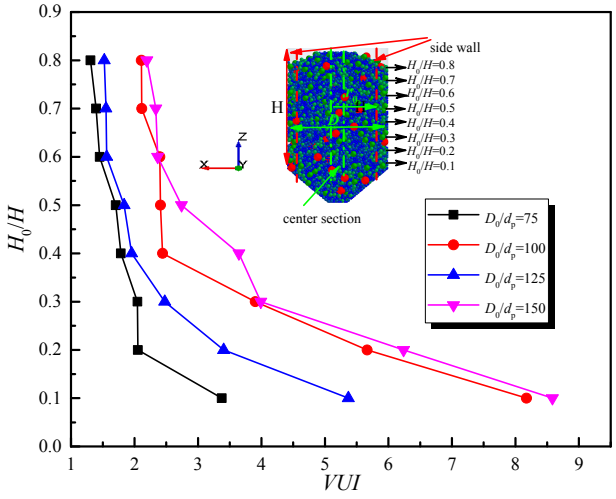


Figure 24. The variation in *VUI* with sinter layers for different geometry factors.

To understand the influence of the geometry factor on the flow pattern in sinter layers, an analysis of the *MFI* of sinter layers with variations in the geometry factor is performed. The variation in *MFI* with sinter layers for different geometry factors is described in Figure 25. It is noted that the magnitude of *MFI* is equal to 0.3 as the criterion of transition from the mass flow to the funnel flow pattern. Evidently, the dimensionless height of the transition of the flow pattern rises and the difference in magnitude of the velocity distribution in the central and sidewall sections increases with an increase in the geometry factor. The results show good consistency with the above conclusion. The uniformity and stabilization of the velocity distribution in sinter layers are gradually disintegrated, leading to a

steady increase in the magnitude of the velocity distribution at identical heights of the sinter layer and a gradual decline in the height of the mass flow pattern with an increase in the geometry factor.

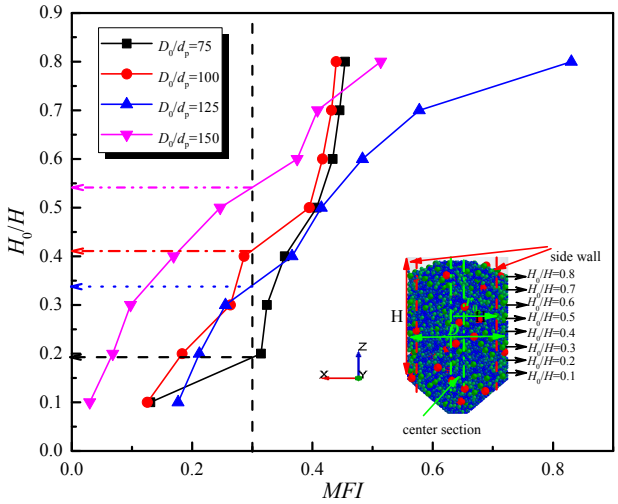


Figure 25. The variation in *MFI* of sinter layers with variations in the geometry factor.

3.5.2. The Effect of the Geometry Factor on Mass Discharge

To better understand the effect of the geometry factor on the performance of mass flow during the discharge process, Figure 26 illustrates the cumulative mass flow as a function of operating time for different geometry factors. Obviously, the cumulative mass export during the operating time interval gradually increases with an increase in the geometry factor, and the rate of the increase slightly decreases with an increase in the geometry factor. With respect to the variation in mass flow rate in the figure inset, the mass flow rate and mean value of mass flow rate gradually increase with an increase in the geometry factor. The mean value of the mass flow rate is 8.76 kg·s^{-1}, 20.81 kg·s^{-1}, 38.68 kg·s^{-1}, and 51.18 kg·s^{-1} for the geometry factor 75, 100, 125, and 150, respectively.

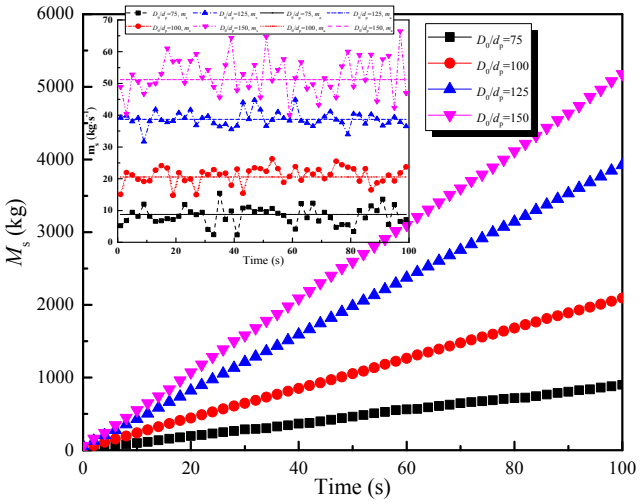


Figure 26. The variation in mass flow during the discharge process with variations in the geometry factor of vertical sinter cooling bed (VSCB). Inset: mass flow rate and mean value of the mass flow rate for different geometry factors.

3.5.3. The Effect of the Geometry Factor on Shear Rate

Figure 27 illustrates a comparison of shear rate with sinter layers as a function of the dimensionless radius direction for different geometry factors of VSCB. The magnitude of the shear rate sharply increases with an increase in the geometry factor. The variation in the magnitude of the shear rate shows a striking rise due to the dramatic reduction of the magnitude of velocity at the sidewall with the increasing geometry factor. The larger magnitude of shear rate shows that the particle flow experiences a large fluctuation in the vicinity of the sidewall, and the sinter particles experience more difficulty in the flow through the passage of VSCB. In terms of the evolution of the magnitude of shear rate in the central section of the flow passage, the magnitude of the shear rate decreases with an increase in the geometry factor because the velocity value continues to exhibit an upward trend with the increase in the geometry factor. It is noteworthy that the shear rate with lower magnitude indicates a trend of a stable smooth flow pattern, while a wider flow passage is observed for the mass flow pattern along the cross-section with an increase in the geometry factor of VSCB.

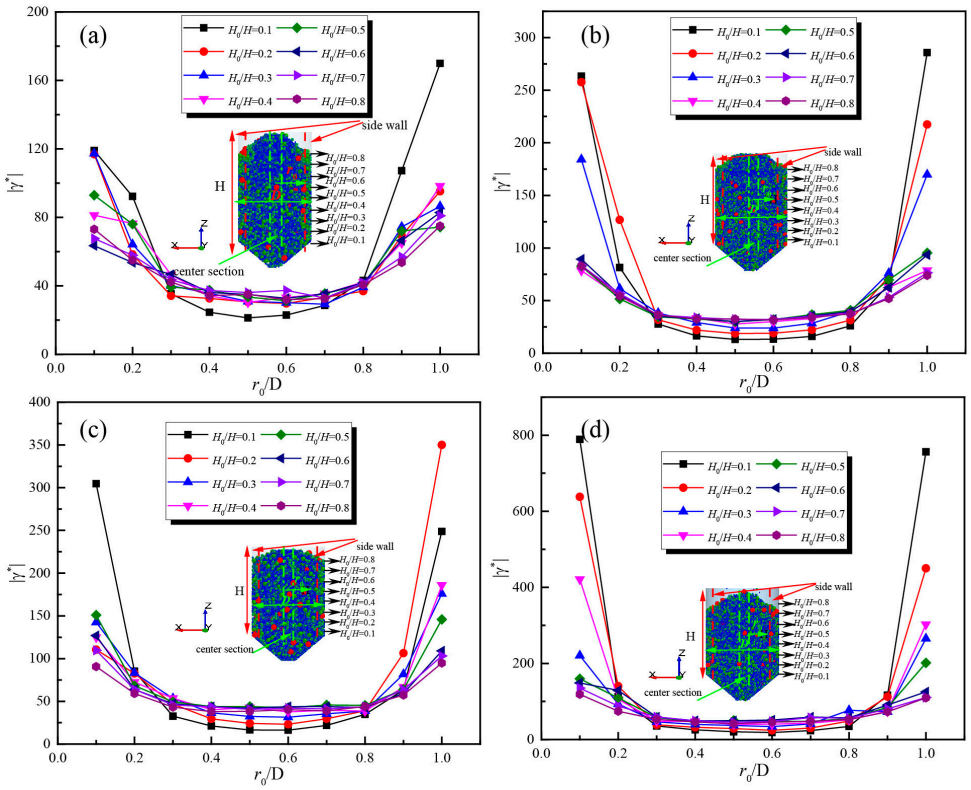


Figure 27. The variation in shear rate of sinter layers with variations in the geometry factor of VSCB of (**a**) D_0/d_p = 75, (**b**) D_0/d_p = 100, (**c**) D_0/d_p = 125, and (**d**) D_0/d_p = 150.

3.6. The Effect of the Discharge Velocity of the Outlet of VSCB

3.6.1. The Effect of the Discharge Velocity of the Outlet of VSCB on Flow Profiles

The driving force of the VSCB discharge is derived from the discharge device, which is composed of an electromagnetic vibrating feeder and rotary seal valve. The sinter particle discharge process is controlled by an external force that develops from the variation in the discharge velocity of the outlet of VSCB (v_0). Figure 28 demonstrates the evolution of sinter layer velocities for different discharge velocities of the VSCB outlet. In terms of the variation in velocity in the central section, the magnitude of velocity witnesses a dramatic rise with acceleration in discharge velocity, but the rate of the increase in velocity gradually decreases. With respect to the evolution of velocity in the vicinity of the sidewall, the magnitude of the velocity gradually accelerates with the increase in discharge velocity and a slight

increase in the rate of the velocity acceleration. The results show that the difference in velocity between the central and sidewall sections experiences a marginal decrease with increasing discharge velocity.

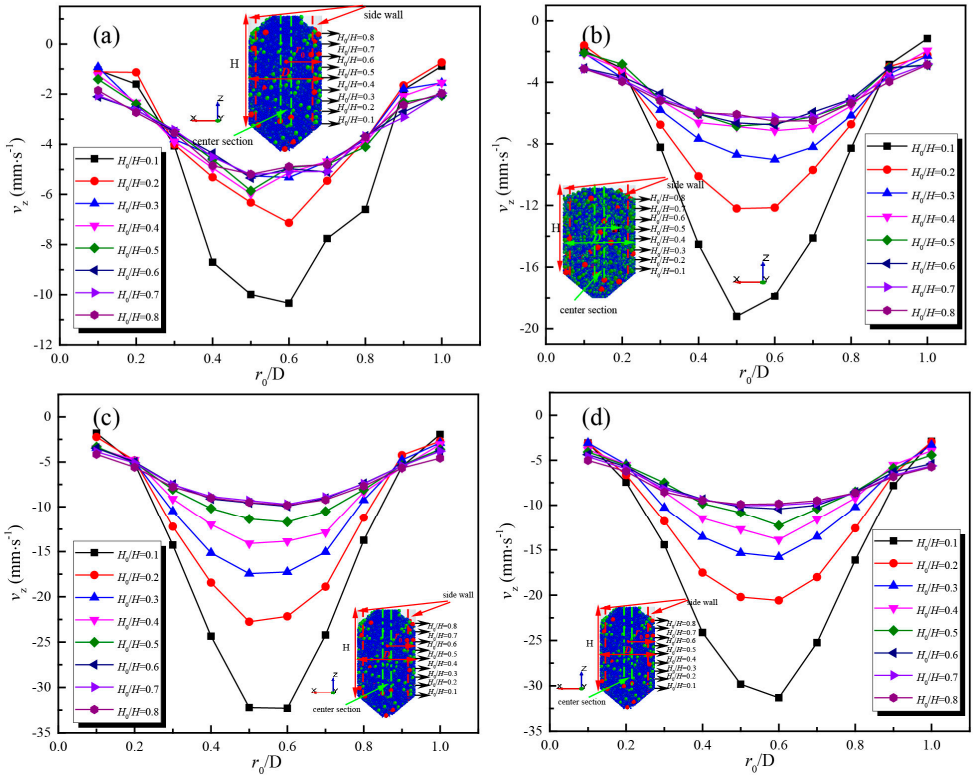


Figure 28. The variation in velocity of all sinter layers for different discharge velocities of outlets of (**a**) v_a = 0.1 m·s^{-1}, (**b**) v_a = 0.2 m·s^{-1}, (**c**) v_a = 0.3 m·s^{-1}, and (**d**) v_a = 0.4 m·s^{-1}.

Moreover, to analyse the velocity distribution in sinter layers with variations of discharge velocity, Figure 29 illustrates the variation in *VUI* as a function of the dimensionless height of sinter layers for different discharge velocities. The difference in velocity distribution between the central and sidewall is clearly greatly increased with increasing discharge velocity, and the same trend occurs in the variation in *VUI* along the height of sinter layers for different discharge velocities. A *VUI* of 0.2 m·s^{-1} for the slight rise in discharge velocity remains nearly identical to that of the *VUI* of 0.1 m·s^{-1} for the discharge velocity. A *VUI* of discharge velocity equal to 0.4 m·s^{-1} is nearly three-fold that of 0.2 m·s^{-1} for the discharge velocity.

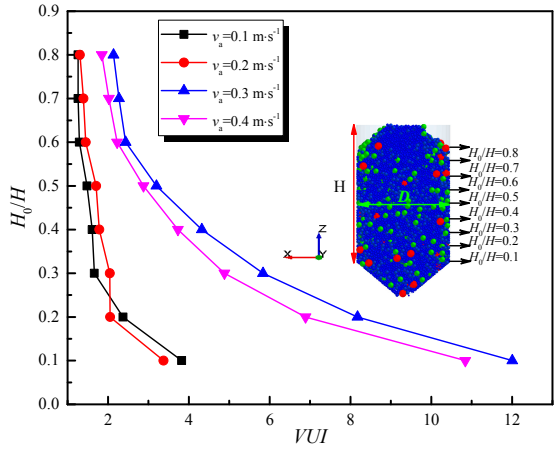


Figure 29. The variation in *VUI* for different sinter layers with different discharge velocities.

To understand the effect of discharge velocity on the variation in the velocity distribution in sinter layers, we focus on the change in velocity in the central and sidewall section of the flow passage of VSCB. Figure 30 reveals the variation in v_c, v_w as a function of the height of sinter layers for different discharge velocities. Regarding the variation in velocity in the vicinity of the sidewall, the magnitude of the velocity increases steeply at the upper height of the sinter layer, and the rate of growth of the magnitude of velocity at the lower height of the sinter layer dramatically increases with an increase in the discharge velocity. The results obtained for the difference in velocity distribution in the sinter layers between central and sidewall sections show a sharp increase with an increase in the discharge velocity. Therefore, it is not a good strategy for improving the performance of sinter flow profiles to simply rely on increasing discharge velocity.

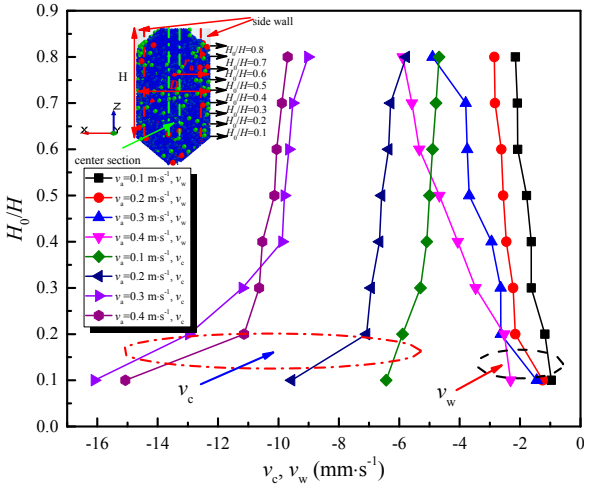


Figure 30. The variation in v_w, v_c along the height of the sinter layers with variations in the discharge velocity.

To further validate the above conclusion and analyse the effect of discharge velocity on the flow pattern of sinter layers, the variation in *MFI* as a function of the dimensionless height of sinter layers for different discharge velocities is described in Figure 31. Evidently, the value of the dimensionless height of sinter layers of the flow pattern in transition declines from 0.35 (a ratio of the calculated height and filling height of the sinter layer) to 0.2 and then begins to increase back to 0.4, and the discharge velocity continues to increase the magnitude of the dimensionless height of sinter layers to remain stable at 0.3. The present research results reveal the height of the mass flow pattern of sinter layers under conditions of a discharge velocity, with an optimal value of 0.2 m·s^{-1}.

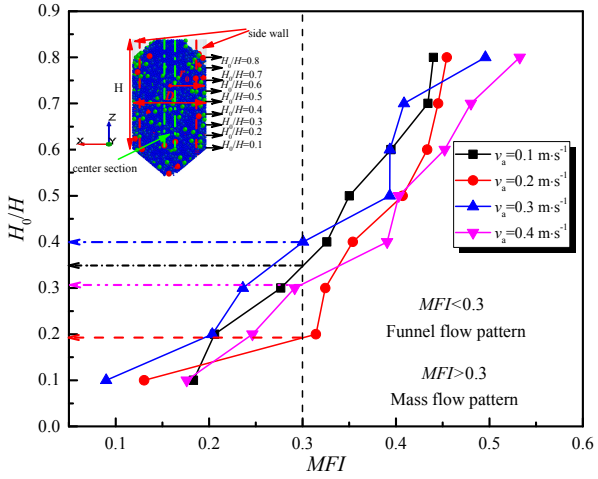


Figure 31. The variation in *MFI* along the height of the sinter layers with variations in the discharge velocity.

3.6.2. The Effect of the Discharge Velocity on Mass Discharge

With respect to the effect of discharge velocity on the cumulative mass export of sinter layers, we quantitatively describe the variation in mass discharge as a function of operating time for variations in the discharge velocity in Figure 32. The variation in cumulative mass export shows a positive linear increase with increasing discharge velocity. The increase in discharge velocity leads to a rate of rising of cumulative mass export acceleration from that time onward.

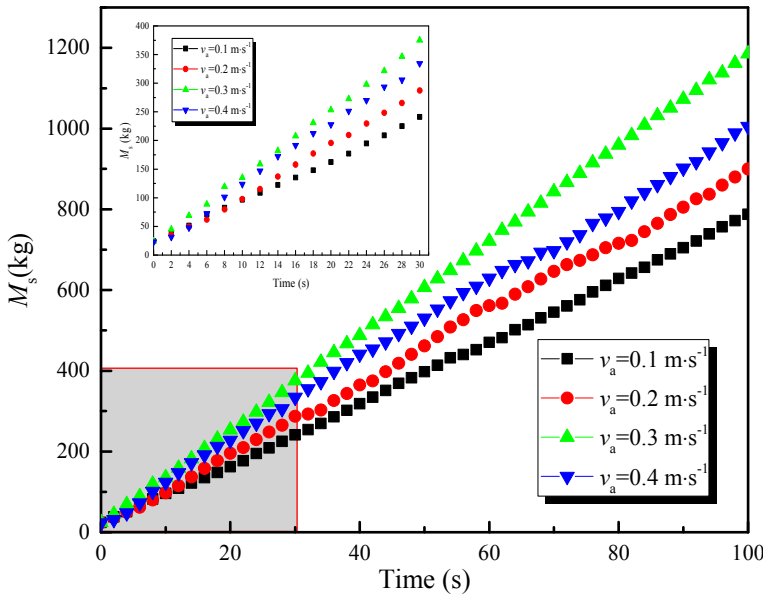


Figure 32. The variation in cumulative mass flow discharge with variations in the discharge velocity. Inset: the variation in cumulative mass export previous to 30 s.

3.6.3. The Effect of the Discharge Velocity on Shear Rate

To comprehensively understand the effect of discharge velocity on the characteristics of variation in shear rate along the radius direction for different heights of sinter layers, we quantitatively and qualitatively analyse the shear rate variation with discharge velocity to clarify the influence of this operating parameter on the flow pattern of sinter layers. Figure 33 shows the dynamic evolution of shear rate along the radius direction in different sinter layers with variations in discharge velocity. The value of the shear rate in the central and sidewall sections clearly declines with an increase in the discharge velocity, as shown in Figure 33. It is possible that the magnitude of velocity in both the sidewall and central section accelerates with increasing discharge velocity, leading to a normal pressure of sinter layers on the sidewall and a reduction of the effect of sidewall and particle resistance and drag with accelerating discharge velocity. Therefore, the difficulty related to particle flow in sinter layers declines with a decrease in the magnitude of the shear rate when the discharge velocity accelerates.

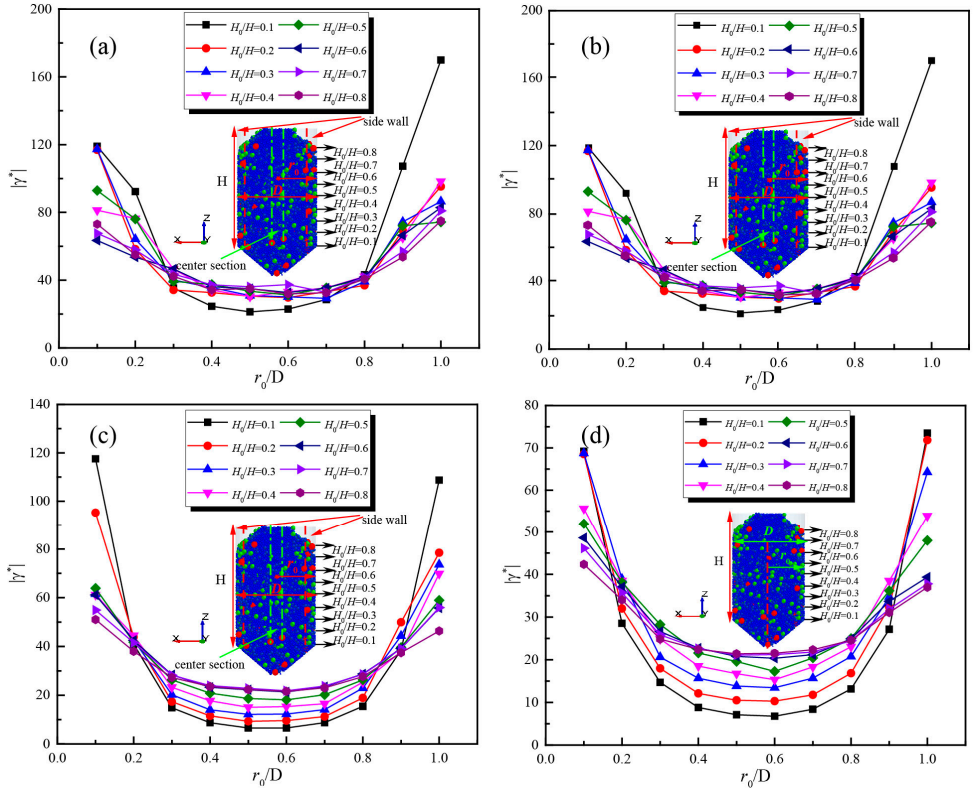


Figure 33. The variation in the shear rate of the sinter layers with variations in the discharge velocity. (**a**) v_a = 0.1 m·s^{-1}, (**b**) v_a = 0.2 m·s^{-1}, (**c**) v_a = 0.3 m·s^{-1}, and (**d**) v_a = 0.4 m·s^{-1}.

3.7. Statistical Analysis Method for Improving the Performance of Flow Profiles in VSCB

3.7.1. Taguchi Method

The Taguchi method provides the advantage of effectively minimizing the number of designs and consideration of full-factorial data to search for the optimal factor and level corresponding to the target response [27–29]. The design factors and their levels exhibit an orthogonal array arrangement in the factorial design experiment. To analyse the effect of different combinations of factors on the target response, the order of importance of factors and their levels is revealed to improve the performance of the design factor combination of the target response. In this study, we have chosen five typical factors, with four levels for each factor having a significant influence on the performance of flow profiles in VSCB. The details for the factors and their levels and units are presented in Table 3; typical factors, including the aspect ratio (H_0/D_0), normalized outlet (d_0/D_0), geometry factor (D_0/d_p), half hopper angle (α), and discharge velocity (v_a), and the value range of their levels are obtained from the actual operation design of the device.

In this section, we mainly focus on the impact of design factors on the dimensionless height of mass flow (h_{mass}) and Froude number (Fr) with the help of the DEM-Taguchi method for VSCB. The dimensionless height of mass flow (h_{mass}) is an essential parameter that provides the ratio of the height of the mass flow (H_0) and the filling height (H) of VSCB to quantitatively describe improvements in the flow pattern performance, benefitting the achievement of the stabilization of sinter layers during the particle flow process. Optimization of the flow pattern is a significant premise for improving the performance of heat transfer in VSCB. The Froude number (Fr) describes the evaluation criteria of the ability of smooth particle flow to solve the problem of particle transportation and ensure smooth particle flow during the gas–solid heat transfer process for enhancing the performance of heat transfer

between sinter particles and air. The Froude number is defined as a formalization of the non-squared symmetric device developed as follows [30,31]:

$$Fr = \frac{m_s}{\rho_b \cdot g^{0.5} \cdot D_0^{2.5}} \tag{10}$$

To investigate the effect of different combinations of design factors on the target responses, an appropriate orthogonal array (16 combinations) is selected to reduce tedious and non-economical calculations from the full factorial calculated 1024 (4^5) combinations, while an evaluation criterion is performed to assess the importance of each factor on the target responses. Therefore, the ratio between signal and noise (*SN*) requires the calculation for the dimensionless height of mass flow (h_{mass}) and Froude number (*Fr*), which are presented as follows. There are three typical modes for evaluating the *SN* ratio, including larger is better, normal is better, and smaller is better. In this study, larger is better for optimizing target responses.

$$SN = 10 \log \frac{1}{n} (\sum {h_{\text{mass}}}^2) \tag{11}$$

$$SN = 10 \log \frac{1}{n} (\sum Fr^2) \tag{12}$$

3.7.2. The Effect of Each Design Factor on the Target Response

The impact of the combination of design factors on the performance of flow profiles of VSCB using the DEM-Taguchi method according to the L_{16} (4^5) orthogonal array and the results of the S/N ratio for the dimensionless height of the mass flow (h_{mass}) and Froude number (*Fr*) are shown in Table 4. The statistical analysis of the performance of each design factor on target responses is shown in Tables 5 and 6 for the dimensionless height of mass flow (h_{mass}) and Froude number (*Fr*), respectively. The performance of each factor and their levels on response is calculated with the aid of Equation (13), taking as an example the calculation process of factor B with level 2: $pf_{B,2}$, including four cases with level 2 of factor B as presented in Equation (13) and the corresponding value of *SN* in Table 4. To calculate the contribution of each factor to the target response, Equation (14) is applied to demonstrate the importance of each design factor on each target response and requires the optimal combination of design factors for improving the flow profiles of VSCB.

$$pf_{i,j} = \frac{1}{n}(SN_{case2} + SN_{case6} + SN_{case10} + SN_{case14})(i = B, j = Level2, n = 4) \tag{13}$$

$$CR_i = \frac{\max(pf_{i,j}) - \min(pf_{i,j})}{\sum_{i}^{5} \sum_{j}^{4} (\max(pf_{i,j}) - \min(pf_{i,j}))} \tag{14}$$

where *i* is the design factor, including A, B, C, D, and E, and *j* is the level of each factor, including the values of 1, 2, 3, 4. The calculated value of the contribution ratio is presented in Tables 5 and 6 for the dimensionless height of mass flow (h_{mass}) and Froude number (*Fr*), respectively.

Table 3. Factors and levels considered in research.

Label	Factor	Level 1	Level 2	Level 3	Level 4
A	Aspect ratio, H_0/D_0 (-)	1	2	3	4
B	Geometry factor D_0/d_p (-)	75	100	125	150
C	Normalized outlet, d_0/D_0 (-)	0.1	0.2	0.3	0.4
D	Half hopper angle, α (°)	30	40	50	60
E	Discharge velocity, v_a ($m \cdot s^{-1}$)	0.1	0.2	0.3	0.4

Table 5 illustrates that the most significant factor is the aspect ratio (H_0/D_0) for the dimensionless height of mass flow (h_{mass}) with a contribution ratio of 31.18%, and the effect of design factors on the target response of h_{mass} follows the contribution ratio of 25.54% for the half hopper angle (α), 19.18% for the geometry factor (D_0/d_p), 13.35% for the normalized outlet scale (d_0/D_0), and 10.75% for the discharge velocity (v_a). Table 5 also illustrates that the rank of the significant design factors on dimensionless mass flow height (h_{mass}) is $H_0/D_0 > \alpha > D_0/d_p > d_0/D_0 > v_a$. Moreover, Figure 34 reveals the effect of each design factor on the dimensionless height performance of mass flow (h_{mass}). It is evident that the optimal combination of design factors is $A_3B_1C_3D_1E_1$, including the aspect ratio (H_0/D_0) with level 3, geometry factor (D_0/d_p) with level 1, normalized outlet scale (d_0/D_0) with level 3, half hopper angle (α) with level 1, and discharge velocity (v_a) with level 1, for improving flow profiles in VSCB.

In terms of the Froude number (*Fr*), Table 6 shows the contribution ratio of each design factor to the target response for the Froude number (*Fr*). The greatest influence of the design factor on *Fr* is the normalized outlet scale (d_0/D_0) with a contribution ratio of 33.81%, followed by the aspect ratio (H_0/D_0) (22.86%), geometry factor (D_0/d_p) (17.73%), discharge velocity (v_a) (17.73%), and half hopper angle (α) (11.83%).

The sequence of influence of design factors on the Froude number (*Fr*) is demonstrated in Table 6 as $d_0/D_0 > H_0/D_0 > D_0/d_p > v_a > \alpha$. A larger value of the mean signal ratio for each factor establishes the optimal combination of design factors, as presented in Figure 35. The optimal combination of design factors providing the smoothest flow export process in VSCB is $A_4B_3C_2D_2E_2$.

Table 4. h_{mass} and *Fr* vary with their S/N ratios for the L_{16} (4^5) orthogonal array.

Parameters	**A**	**B**	**C**	**D**	**E**	**Results**		**SN Ratio**	
Case	Levels					h_{mass}	*Fr*	h_{mass}	Froude
1	1	1	1	1	1	0.8	0.011453	−1.93820	−38.8216
2	1	2	2	2	2	0.55	0.050536	−5.19275	−25.9280
3	1	3	3	3	3	0.6	0.043514	−4.43697	−27.2274
4	1	4	4	4	4	0.466	0.02666	−6.63228	−28.6367
5	2	1	2	3	4	0.8	0.035295	−1.93820	−29.0457
6	2	2	1	4	3	0.625	0.006092	−4.08240	−30.2042
7	2	3	4	1	2	1	0.041325	0	−27.6757
8	2	4	3	2	1	0.866	0.03038	−1.24964	−30.3482
9	3	1	3	4	2	0.955	0.039063	−0.39993	−26.7776
10	3	2	4	3	1	0.95	0.021707	−0.44553	−33.2680
11	3	3	1	2	4	0.733	0.028412	−2.69792	−30.9300
12	3	4	2	1	3	0.8421	0.054712	−1.49273	−25.2383
13	4	1	4	2	3	1	0.04594	0	−26.7562
14	4	2	3	1	4	1	0.048705	0	−26.2485
15	4	3	2	4	1	0.7	0.066169	−3.09804	−23.5869
16	4	4	1	3	2	0.708	0.03728	−2.99933	−28.5705

Table 5. Factorial effect of h_{mass}.

Level	**A**	**B**	**C**	**D**	**E**
1	−4.55	−1.07	−2.93	−0.86	−1.68
2	−1.82	−2.43	−2.93	−2.28	−2.15
3	−1.26	−2.56	−1.52	−2.45	−2.50
4	−1.52	−3.10	−1.77	−3.55	−2.82
Delta	3.29	2.02	1.41	2.70	1.13
Rank	1	3	4	2	5
Contribution (%)	31.18	19.18	13.35	25.54	10.75

Table 6. Factorial effect of *Fr*.

Level	A	B	C	D	E
1	−30.86	−30.70	−35.66	−29.50	−31.51
2	−32.84	−32.44	−25.95	−28.49	−27.58
3	−29.40	−27.36	−28.00	−29.53	−30.88
4	−26.29	−28.91	−29.80	−31.88	−29.43
Delta	6.55	5.08	9.71	3.39	3.92
Rank	2	3	1	5	4
Contribution (%)	22.86	17.73	33.89	11.83	13.68

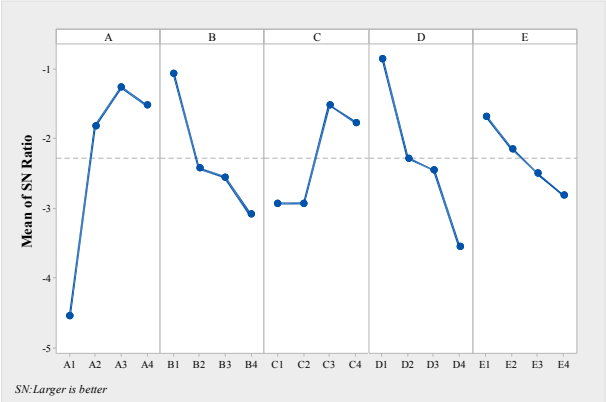


Figure 34. The effect of each design factor on h_{mass}.

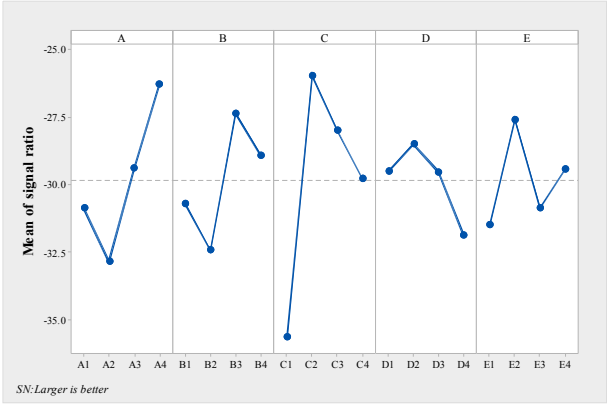


Figure 35. The effect of each design factor on *Fr*.

4. Conclusions

To comprehensively understand the influence of structural factors (aspect ratio, geometry factor, normalized outlet scale, and half hopper angle) and the operating factor (discharge velocity) on the characteristics of the flow pattern in VSCB, the effect of individual factors on flow profiles, mass flow rate, and shear rate is assessed during the particle flow process using the discrete element method (DEM), while the significant and contribution ratio of each factor to the target response and the optimal combination of design factors are investigated using the Taguchi method. Several conclusions are listed as follows.

With respect to the aspect ratio, the contrast of the velocity in sinter layers is even sharper and then declines prior to the return to the nearly original value with an increase in the aspect ratio. Regarding the effect of the aspect ratio on the variation in the height of mass flow and mass flow rate, the trend is mirrored in the study. The magnitude of the shear rate increases and then decreases before steeply rising with aspect to the increase in the ratio.

Regarding the geometry factor, the magnitude of velocity in the vicinity of the sidewall is greatly reduced, and the corresponding value in the central section of the sinter layers is dramatically accelerated with an increase in the geometry factor. The mass flow rate in VSCB steeply increases with the increase in geometry factor, but the opposite trend is observed in the variation in mass flow height. In terms of the variation in shear rate, a slight increase in shear rate is observed in the central section of the sinter layers, and the corresponding value grows more substantially in the sidewall section.

Concerning the normalized outlet scale, the difference in velocity distribution among sinter layers increases, but the rate of rising gradually decreases with the increase in normalized outlet scale. With respect to the height of mass flow and mass flow rate, a similar trend is recorded, with both showing an increase with an increase in the normalized outlet scale. The particle flow difficulty in sinter layers is improved with an increase in the normalized outlet scale.

Upon closer inspection, the velocity distribution in the central section of the sinter layer accelerates, and an opposite trend is observed in the vicinity of the sidewall with an increase in the half hopper angle. The stabilization and uniformity of sinter layers gradually decrease with an increase in the half hopper angle. The mass flow height and mass flow rate increase with decreases in the half hopper angle. The variation in the magnitude of shear rate presents a completely different trend between the central sidewall sections of sinter layers, the shear rate value is nearly stable in the central section, and the corresponding value in the sidewall section experiences a steep increase with increases in the half hopper angle.

In terms of discharge velocity, the variation in velocity distribution in different sections of the sinter layers shares the same trend of increase with an increase in discharge velocity. The uniformity and stabilization of sinter layers slightly decrease with increases in the discharge velocity. The impact of discharge velocity on the variation in the height of mass flow experiences a minor fluctuation, showing that the increasing discharge velocity with a negative correlation varies with the mass flow height. However, the variation in the mass flow rate of the sinter layers shows the opposite trend. Regarding the difficulty of improving the smooth flow in sinter layers, the magnitude of the shear rate of entire sinter layers decreases gradually with the increase in the discharge velocity.

To analyse the influence of design factors on the target response, the Taguchi method is applied to examine the significance of design factors on improving the performance of flow profiles in VSCB. The results show that the sequence of the importance of design factors on h_{mass} is $H_0/D_0 > \alpha > D_0/d_{\mathrm{p}} > d_0/D_0 > v_{\mathrm{a}}$, while the optimal combination of design factors for h_{mass} is $\mathrm{A_3B_1C_3D_1E_1}$. Regarding the Froude number (Fr), the most significant factor is the normalized outlet scale (d_0/D_0), followed by the factor aspect ratio (H_0/D_0), geometry factor (D_0/d_{p}), discharge velocity (v_{a}), and half hopper angle (α). The optimal combination of design factors for Fr is $\mathrm{A_4B_3C_2D_2E_2}$.

Author Contributions: Conceptualization, J.C. and J.F.; methodology, J.F.; software, J.F.; validation, J.F.; formal analysis, J.F.; investigation, J.F.; resources, J.C.; data curation, J.C.; writing—original draft preparation, J.F.; writing—review and editing, J.F. and J.C.; visualization, J.F. and J.C.; supervision, J.C.; project administration, J.C.; funding acquisition, J.C. All authors have read and agreed to the published version of the manuscript.

Funding: This research is funded by National Key R&D (research and development) Program of China, grant number 2017YFB0304200 and the National Natural Science Foundation of China, grant number 51734004.

Conflicts of Interest: The authors declare no conflict of interest.

Nomenclature

m_i	Mass of particle i (kg)
v_i	Translational velocity of particle i ($\mathrm{m{\cdot}s^{-1}}$)
i	Particle i
t	Time (s)
g	Gravitational acceleration ($\mathrm{m{\cdot}s^{-2}}$)
n_i	Number of contact particles
${F_c}^n$	Normal contact force (N)
${F_d}^n$	Normal damping force (N)

$F_c{}^t$	Tangential contact force (N)
$F_d{}^t$	Tangential contact force (N)
I_i	Inertial moment of particle i (kg·m^{-2})
ω_i	Angular velocity of particle i (rad·s^{-1})
$T_{t,ij}$	Tangential torque (N·m)
$T_{r,ij}$	Rolling friction torque (N·m)
E^*	Equivalent young's modulus (MPa)
r^*	Equivalent radius (m)
δ_n	Overlap distance of two particles (m)
$\mathbf{n_{ij}}$	Normal unit vector (-)
υ	Poisson's ratio (-)
G^*	Equivalent shear modulus (MPa)
$\mathbf{t_{ij}}$	Tangential unit vector (-)
e	Restitution coefficient (-)
S_n	Normal elastic constant coefficient (MPa·m^{-2})
S_t	Tangential elastic constant coefficient (MPa·m^{-2})
r_{ij}	Contact radius of two particles (m)
$\boldsymbol{n}$	Normal direction component (-)
$\boldsymbol{t}$	Tangential direction component (-)
m^*	Equivalent mass (kg)
μ	Coefficient of particles friction (-)
$v_{ij}{}^t$	Tangential velocity (m·s^{-1})
$v_{ij}{}^n$	Normal velocity (m·s^{-1})
$\omega_{t,ij}$	Tangential angular velocity of particle i (rad·s^{-1})
r	Error value (%)
$f_{\mathrm{cal},i}$	Calculation results in the ith case (kg·s^{-1})
$f_{\mathrm{exp},i}$	Experiment results in the ith case (kg·s^{-1})
v_{w}	Velocity of the sidewall (mm·s^{-1})
v_{c}	Velocity of the central section (mm·s^{-1})
m_s	Average mass flow rate (kg·s^{-1})
VUI_j	Velocity uniformity index in the jth layer
v_{jk}	Velocity of the kth column in the jth layer (mm·s^{-1})
$v_{ave,j}$	Velocity of the jth layer (mm·s^{-1})
v_r	Velocity of the rth time step in operating time (mm·s^{-1})
r_{ij}	Shear stress of unit element (MPa)
$\lvert r^* \rvert$	Shear rate tensor
ρ_b	Bulk density of sinter layers (kg·m^3)
D_0	Dimension of the outlet of VSCB (mm)
G	Acceleration of gravity of mass (m·s^{-2})
h_{mass}	Normalized height of mass flow pattern
n	Total number of experiments
α	Half hopper angles (°)
v_{a}	Discharge velocity (m·s^{-1})
CR	Contribution ratio
pf	Performance factor of a factor with its level

Subscripts

i	Element of design factor
j	Element of design factor
k	The number of columns in the sinter layer
m	Total number of columns in identity layers
s	Total operating time
c	Contact
d	Damping

t	Tangential
r	Rolling
cal	Calculation
exp	Experiment
w	Wall
c	Central
ave	Average

Abbreviate

DEM	Discrete element method
CFD	Computational fluid dynamics
VSCB	Vertical sinter cooling packed bed
VUI	Velocity uniformity index
MFI	Mass flow index
Fr	Froude number
PIV	Particle image velocimetry
SN	Signal noise

References

1. Pan, L.; Wei, X.; Peng, Y.; Ma, Y.; Li, B. Theoretical study on the cooling procedure for vertical flow sinters. *Appl. Therm. Eng.* **2017**, *127*, 592–601. [CrossRef]
2. Feng, J.; Zhao, L.; Zhang, S.; Dong, H. Exergy analysis and parameter optimization of sinter cooling process in vertical moving bed for waste heat recovery. *Appl. Therm. Eng.* **2020**, *175*, 115370. [CrossRef]
3. Zhang, S.; Zhao, L.; Feng, J.; Luo, X.; Dong, H. Thermal analysis of sinter vertical cooler based on waste heat recovery. *Appl. Therm. Eng.* **2019**, *157*, 113708. [CrossRef]
4. Feng, J.; Zhang, S.; Dong, H.; Pei, G. Frictional pressure drop characteristics of air flow through sinter bed layer in vertical tank. *Powder Technol.* **2019**, *344*, 177–182. [CrossRef]
5. Cheng, Z.; Guo, Z.; Tan, Z.; Yang, J.; Wang, Q. Waste heat recovery from high-temperature solid granular materials: Energy challenges and opportunities. *Renew. Sustain. Energy Rev.* **2019**, *116*, 109428. [CrossRef]
6. Tian, F.-Y.; Huang, L.-F.; Fan, L.-W.; Qian, H.-L.; Gu, J.-X.; Yu, Z.-T.; Hu, Y.-C.; Ge, J.; Cen, K.-F. Pressure drop in a packed bed with sintered ore particles as applied to sinter coolers with a novel vertically arranged design for waste heat recovery. *J. Zhejiang Univ. A* **2016**, *17*, 89–100. [CrossRef]
7. Leong, J.; Jin, K.-W.; Shiau, J.-S.; Jeng, T.-M.; Tai, C.H. Effect of sinter layer porosity distribution on flow and temperature fields in a sinter cooler. *Int. J. Miner. Met. Mater.* **2009**, *16*, 265–272. [CrossRef]
8. Pan, L.; Wei, X.-L.; Peng, Y.; Shi, X.-B.; Liu, H.-L. Experimental study on convection heat transfer and air drag in sinter layer. *J. Central South. Univ.* **2015**, *22*, 2841–2848. [CrossRef]
9. Feng, J.; Zhang, S.; Dong, H.; Pei, G. Effect of gas inlet parameters on exergy transfer performance of sinter cooling process in vertical moving bed. *Appl. Therm. Eng.* **2019**, *152*, 126–134. [CrossRef]
10. Feng, J.-S.; Dong, H.; Gao, J.-Y.; Liu, J.-Y.; Liang, K. Exergy transfer characteristics of gas-solid heat transfer through sinter bed layer in vertical tank. *Energy* **2016**, *111*, 154–164. [CrossRef]
11. Liu, Z.; Feng, Y.; Zhang, X.; Xu, L.; Yu, Z. Numerical and experimental study on coke size distribution in bell-type charging in the CDQ shaft. *J. Univ. Sci. Technol. Beijing, Miner. Met. Mater.* **2008**, *15*, 236–240. [CrossRef]
12. Feng, Y.; Zhang, X. Experimental and numerical investigations of cokes descending behaviour in a coke dry quenching cooling shaft. *Appl. Therm. Eng.* **2008**, *28*, 1485–1490.
13. Yu, X.; Shen, Y. Model study of central coke charging on ironmaking blast furnace performance: Effects of charing pattern and nut coke. *Powder Technol.* **2020**, *361*, 124–135. [CrossRef]
14. Qiu, L.; Sang, D.; Feng, Y.; Huang, H.; Zhang, X. Study on heat transfer of process intensification in moving bed reactor based on the discrete element method. *Chem. Eng. Process. Process. Intensif.* **2020**, *151*, 107915. [CrossRef]
15. Song, B.; Feng, Y.; Zhang, X. Numerical study on pressure drop factor in the vent-cap of CDQ shaft. *J. Therm. Sci.* **2008**, *17*, 69–76. [CrossRef]

16. Zhang, Y.; Jia, F.; Zeng, Y.; Han, Y.; Xiao, Y. DEM study in the critical height of flow mechanism transition in a conical silo. *Powder Technol.* **2018**, *331*, 98–106. [CrossRef]
17. Zeng, Y.; Jia, F.; Zhang, Y.; Meng, X.; Han, Y.; Wang, H. DEM study to determine the relationship between particle velocity fluctuations and contact force disappearance. *Powder Technol.* **2017**, *313*, 112–121. [CrossRef]
18. Han, Y.; Jia, F.; Li, G.; Liu, H.; Li, J.; Chen, P. Numerical analysis of flow pattern transition in a conical silo with ellipsoid particles. *Adv. Powder Technol.* **2019**, *30*, 1870–1881. [CrossRef]
19. Fullard, L.; Davies, C.; Neather, A.; Breard, E.; Godfrey, A.; Lube, G. Testing steady and transient velocity scalings in a silo. *Adv. Powder Technol.* **2018**, *29*, 310–318. [CrossRef]
20. Chen, J.F.; Rotter, J.M. Correlation between the flow pattern and wall pressures in a full scale experiment silo. *Eng. Struc.* **2007**, *29*, 2308–2320.
21. Job, N.; Dardenne, A.; Pirard, J.-P. Silo flow-pattern diagnosis using the tracer method. *J. Food Eng.* **2009**, *91*, 118–125. [CrossRef]
22. Cundall, P.; Strack, O. Modeling of Microscopic Mechanisms in Granular Material. *Stud. Appl. Mech.* **1983**, *7*, 137–149. [CrossRef]
23. Aleshin, V.V.; Abeele, K.V.D. Preisach analysis of the Hertz–Mindlin system. *J. Mech. Phys. Solids* **2009**, *57*, 657–672. [CrossRef]
24. Aleshin, V.; Abeele, K.V.D. General solution to the Hertz–Mindlin problem via Preisach formalism. *Int. J. Non-Linear Mech.* **2013**, *49*, 15–30. [CrossRef]
25. Staron, L.; Lagrée, P.-Y.; Popinet, S. The granular silo as a continuum plastic flow: The hour-glass vs. the clepsydra. *Phys. Fluids* **2012**, *24*, 103301. [CrossRef]
26. Midi, G. On dense granular flows. *Eur. Phys. J. E* **2004**, *14*, 341–365. [CrossRef]
27. Sadeghifam, A.N.; Meynagh, M.M.; Tabatabaee, S.; Mahdiyar, A.; Memari, A.; Ismail, S. Assessment of the building components in the energy efficient design of tropical residential buildings: An application of BIM and statistical Taguchi method. *Energy* **2019**, *188*, 116080. [CrossRef]
28. Hajji, H.; Nasr, S.; Millot, N.; Ben Salem, E. Study of the effect of milling parameters on mechanosynthesis of hydroxyfluorapatite using the Taguchi method. *Powder Technol.* **2019**, *356*, 566–580. [CrossRef]
29. Shu, L.; Yang, M.; Zhao, H.; Li, T.; Yang, L.; Zou, X.; Li, Y. Process optimization in a stirred tank bioreactor based on CFD-Taguchi method: A case study. *J. Clean. Prod.* **2019**, *230*, 1074–1084. [CrossRef]
30. Lehmann, H.J. Ein Beitrag zur Untersuchung des Einflusses der Schuttguteigenchaften und der Bwhaltergeometrie auf Massendurchdatz beim Ausflieben von Schuttgut aus Zylindrischen Behaltern. Ph.D. Thesis, Wirtschaft und Kultur Leipzig, Weimar, Germany, 1978.
31. Mellmann, J.; Hoffmann, T.; Furll, C. Mass flow during unloading of agricultural bulk materials from silos depending on particle form, flow properties and geometry of the discharge opening. *Powder Technol.* **2014**, *253*, 46–52. [CrossRef]



© 2020 by the authors. Licensee MDPI, Basel, Switzerland. This article is an open access article distributed under the terms and conditions of the Creative Commons Attribution (CC BY) license (http://creativecommons.org/licenses/by/4.0/).